Delft University of Technology

Design of a modular heat storage for heat commodification

Optimal aspect ratio of a laterally heated PCM enclosure

Zhao, Luoguang; Zhao, Chunrong; Opolot, Michael; Mancin, Simone; Hooman, Kamel

DOI
10.1016/j.energy.2025.139420

Publication date
2025

Document Version
Final published version

Published in
Energy

Citation (APA)
Zhao, L., Zhao, C., Opolot, M., Mancin, S., & Hooman, K. (2025). Design of a modular heat storage for heat commodification: Optimal aspect ratio of a laterally heated PCM enclosure. *Energy*, *341*, Article 139420. https://doi.org/10.1016/j.energy.2025.139420

Important note
To cite this publication, please use the final published version (if applicable).
Please check the document version above.

Copyright
Other than for strictly personal use, it is not permitted to download, forward or distribute the text or part of it, without the consent of the author(s) and/or copyright holder(s), unless the work is under an open content license such as Creative Commons.

Takedown policy
Please contact us and provide details if you believe this document breaches copyrights.
We will remove access to the work immediately and investigate your claim.

This work is downloaded from Delft University of Technology.
For technical reasons the number of authors shown on this cover page is limited to a maximum of 10.

Energy 341 (2025) 139420

Contents lists available at ScienceDirect

Energy

journal homepage: www.elsevier.com/locate/energy

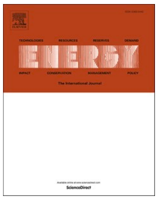

Design of a modular heat storage for heat commodification: Optimal aspect ratio of a laterally heated PCM enclosure

Luoguang Zhao [a,b], Chunrong Zhao [c,*], Michael Opolot [d], Simone Mancin [e], Kamel Hooman [f]

[a] School of Mechanical Engineering, Hubei University of Technology, Wuhan, 430068, China
[b] School of Engineering and Materials Science, Queen Mary University of London, London, E1 4NS, UK
[c] School of Aerospace, Mechanical and Mechatronic Engineering, The University of Sydney, NSW, 2006, Australia
[d] Centre for Hydrogen and Renewable Energy, Central Queensland University, Gladstone, QLD, Australia
[e] Department of Management and Engineering, University of Padova, Stradella S. Nicola, 3, Vicenza, 36100, Italy
[f] Department of Process and Energy, Delft University of Technology, Leeghwaterstraat 39, 2628 CB, Delft, the Netherlands

ARTICLE INFO

Keywords:
Melting and solidification
Optimal aspect ratio
Convective enhancement factor
Scale analysis

ABSTRACT

In this work, we numerically investigate a rectangular PCM tank with isothermal heating applied to one vertical wall, while the remaining walls are insulated. The effects of enclosure length (L) and height (H) on melting performance are systematically examined. It is shown that for each length, there exists an optimal height that minimizes the melting time. Moreover, this optimal height H_{opt} decreases with increasing enclosure length and wall temperature. A theoretical model is developed and validated against simulation results, revealing that the optimal enclosure aspect ratio follows the scaling law $AR_{opt} \sim Ra_L^{-1/7}$. This framework provides practical guidance for the design of insert-free PCM enclosures aimed at rapid thermal response and efficient energy storage.

Nomenclature

c_p	Specific heat capacity, J/kg·K	μ	Dynamic viscosity, Pa·s
C	Mushy zone constant, kg/m^3·s	ν	Kinematic viscosity, m^2/s
C_H	Multiplier for Eq. (16)	ω	Convection enhancement factor, -
g	Gravitational acceleration, m/s^2	δ	Boundary layer thickness, m
H	Enclosure height, m	**Subscript**	
h_{sf}	Latent heat, J/kg	l	Liquid or liquidus
k	Thermal conductivity, W/m·K	m	Melting point
K_t	The slope for Eq. (10b)	s	Solid or solidus
L	Enclosure length, m	opt	Optimal
Nu	Nusselt number	w	Wall
q	Heat transfer rate, W	cond	Conduction
q''	Heat flux, W/m^2	0	Initial
Q	Thermal energy, J	**Abbreviation**	
Ra	Rayleigh number	AR	Aspect ratio
Ste	Stefan number	CFD	Computational fluid dynamics
T	Temperature, K	PCM	Phase change material
t_{melt}	Melting time, min	PRESTO!	Pressure staggering option
t_{solid}	Solidification time, min	QUICK	Quadratic upstream interpolation for convective kinetics
Greek letter			
α	Thermal diffusivity, m^2/s	SIMPLE	Semi-implicit method for pressure linked equations
β	Thermal expansion coefficient, 1/K		
γ	Liquid fraction	TES	Thermal energy storage
ρ	Density, kg/m^3	TRL	Technological readiness level

(continued on next column)

(continued)

1. Introduction

The efficiency of energy utilization across industrial, commercial, and residential sectors remains fundamentally constrained by thermodynamic and practical limitations, leading to the inevitable generation of waste heat. Globally, a substantial fraction of input energy—often exceeding 50 %—is lost as low-grade thermal energy [1]. As energy systems transition toward decarbonization and improved sustainability, the recovery and valorisation of waste heat [2] have emerged as pivotal strategies. One promising pathway is the *commodification of heat* [3], where waste thermal energy is transformed into a tradable and

---

* Corresponding author.
E-mail address: chunrong.zhao@sydney.edu.au (C. Zhao).

https://doi.org/10.1016/j.energy.2025.139420
Received 3 August 2025; Received in revised form 5 September 2025; Accepted 21 November 2025
Available online 22 November 2025
0360-5442/© 2025 The Authors. Published by Elsevier Ltd. This is an open access article under the CC BY license (http://creativecommons.org/licenses/by/4.0/).

dispatchable resource. Central to this vision is the deployment of modular thermal energy storage (TES) technologies capable of decoupling heat generation from consumption in both time and location [4]. Among different TES technologies, latent heat TES systems employing phase change materials (PCMs) offer notable advantages, including high volumetric energy density, near-isothermal operation, and minimal thermal loss during storage [5].

Despite their potential, one of the most critical challenges facing PCM-based thermal energy storage systems is the inherently low thermal conductivity of most phase change materials [6], which significantly slows the melting/solidification processes and impairs the system's thermal responsiveness. Consequently, there is a substantial body of research aimed at accelerating the heat transfer rate during phase change [7–9]. Tao et al. [10] broadly classified enhancement strategies into three categories: improving the thermal conductivity of PCM composites, increasing the heat transfer surface area, and enhancing melting uniformity. For the first category, common approaches include embedding the PCM into thermally conductive porous matrices such as metal [11] or graphite [12] foams, or dispersing nanoparticles or nanomaterials within the PCM at controlled concentrations [13,14]. The second approach focuses on augmenting heat transfer surface area using internal fin structures—such as straight [15], tree-shaped [16], or helical [17] fins—or encapsulating the PCM in various capsule configurations [18,19]. The third category involves cascaded PCM arrangements [20,21], where multiple materials with successively lower melting points are layered to promote uniform melting along the streamwise direction. While many of these techniques have been shown to significantly improve heat transfer performance, they often introduce additional mass or volume, thereby reducing the overall energy storage density. This trade-off highlights the need for advanced designs that can simultaneously enhance heat transfer while maintaining compactness and high energy capacity [22].

In many practical applications, PCM enclosures fail to achieve optimal melting performance due to mismatches between geometric design and phase change dynamics. According to constructal theory [23], "for a finite-size flow system to persist in time (to live), it must evolve such that it provides greater and greater access to the currents that flow through it." This principle suggests that, under certain conditions, a well-designed finless PCM enclosure may outperform finned configurations by preserving natural convection pathways. Experimental evidence supporting this was provided by Kamkari et al. [24], who observed that a rectangular PCM cell heated isothermally from the bottom (0° inclination) exhibited a faster melting rate than the same geometry with three inserted fins heated from the side (90° inclination). In the latter case, the melting process was hindered by a phenomenon termed the "shrinking solid regime" [25], in which the melt front contracts toward the heated wall, significantly delaying complete phase change—sometimes accounting for nearly half of the melting duration [26]. Theoretical predictions based on simplified models suggest that the melting time of side-heated enclosures should scale inversely with height to the power of 7/4 [27]. However, numerical results reported by Vogel et al. [28] contradict this trend, showing that increasing the enclosure height prolongs the melting time. This discrepancy has not been reconciled in the literature and points to the existence of a critical enclosure height or aspect ratio (*AR*) that minimizes melting duration under lateral heating. Identifying and quantifying this geometric threshold remains an open and practically relevant research question.

Over the past decades, a growing body of literature has examined the influence of enclosure aspect ratio (AR) on the melting performance of phase change material (PCM) systems. For bottom-heated enclosures, Ye [29] demonstrated that increasing AR (0.1–10) enhanced buoyancy-driven convection and significantly reduced melting time, particularly beyond AR = 1. Yang et al. [30,31] extended this analysis by evaluating multiple inclination angles and reported that melting time increased with AR (0.1–8.0) under both bottom and lateral heating configurations. In subsequent work incorporating metal foam, the same authors found that this trend persisted and that inclination effects became negligible, owing to the dominance of conduction. Under constant heat flux boundaries, Xie and Wu [32] observed a local optimum near AR ≈ 0.2–0.3 for lateral heating, beyond which melting time increased; in contrast, bottom heating exhibited only a mild dependence on AR across a range of 0.167–6. He et al. [33] investigated partially filled copper foam–PCM systems under lateral heating with constant enclosure volume and reported that while melting time generally decreased with increasing AR (1–10), the most significant enhancement—corresponding to a 22.6 % increase in thermal energy storage (TES) rate density—was observed at AR = 2, with diminishing returns thereafter. Elbahjaoui and El Qarnia [34] examined lateral heating of a nanoparticle-enhanced PCM (NEPCM) slab under convective boundary conditions with fixed Reynolds number and Rayleigh number (Ra) and found that melting time decreased with AR (0.5–16); to maintain constant Ra, the characteristic length was scaled as $l_0 \propto H/\sqrt{AR}$. A distinct set of studies identified explicit optimal ARs. Hamad et al. [35] experimentally and numerically analysed PEG 1500 melting in enclosures with constant height and constant volume, identifying a consistent global optimum at AR = 2.3. Similarly, Behbahan et al. [36] studied copper foam–PCM composites and found that the optimal AR increased exponentially with porosity—from AR = 1.27 at 85 % to AR = 4.2 at 95 %—under both constant volume and constant PCM mass constraints. While these studies have identified discrete optimal AR values for specific configurations, a generic theoretical prediction of the optimal AR remains absent in the literature, and the underlying heat transfer mechanisms governing this geometric optimum are yet to be comprehensively unravelled.

Whilst the interplay between conduction and convection heat transfer is the core to this research question [37], relevant research with regard to melting with thermal enhancing inserts following identical heat transfer principle can be referred. Several prior studies have sought to optimize the design of extended surface structures, such as fins and porous media, to enhance the melting performance of PCM enclosures. In the case of annular fins embedded in a vertical cylindrical tank, Yang et al. [38] reported that melting time followed a parabolic trend with respect to fin number under a fixed fin volume fraction (2 %), identifying 31 as the optimal fin count. A similar parabolic pattern was observed in horizontally oriented PCM enclosures with longitudinal straight fins [39]. To investigate the underlying mechanism, Zhao et al. [15] conducted a numerical analysis on bottom-heated rectangular enclosures containing straight fins, deriving theoretical correlations for optimal fin spacing and length by analysing the competing roles of conduction and natural convection. These insights also extend to porous structures. Sundarram et al. [40] demonstrated that reducing the pore size in microcellular metal foams (<0.1 mm) improved effective thermal conductivity but suppressed natural convection entirely. In contrast, Parida [41] showed that foams with larger pores (3–6 mm) allowed convective effects to re-emerge, leading to a non-monotonic, parabolic dependence of melting time on pore size. This trend has been corroborated in periodic structures with characteristic cell sizes between 2.54 and 12.7 mm [9,42]. Additional studies have explored how porosity, thermal diffusivity, enclosure length, and orientation influence the critical cell size that minimizes melting duration [37]. While these mechanisms have been extensively characterized for systems incorporating extended surfaces such as fins or porous matrices, the existence and origin of a similar optimum in finless PCM enclosures remain insufficiently clarified. Addressing this fundamental gap—by identifying and explaining the optimal aspect ratio based on underlying heat transfer mechanisms—forms the core objective of the present study.

The remainder of this paper is structured as follows. Section 2 introduces the numerical model developed for simulating the melting process in side-heated PCM enclosures and presents its validation against experimental data available in the literature. In Section 3, a parametric study is conducted to identify the turning point of enclosure height that minimizes melting time across different aspect ratios and boundary temperatures. Section 4 presents a theoretical analysis based on scaling arguments, from which empirical correlations are derived and validated using the numerical results. Finally, Section 5 summarizes the main conclusions and key insights of the study and outlines potential directions for future work.

2. Methodology

2.1. Physical model

A two-dimensional rectangular enclosure filled with phase change material (PCM) is considered, as illustrated in Fig. 1. The enclosure is isothermally heated from one vertical sidewall, while the opposite vertical wall and the top and bottom surfaces are assumed adiabatic. The objective of this study is to investigate and optimize the enclosure height (H) in order to maximize the bulk melting rate, with the enclosure length (L) fixed at 25 mm, 50 mm, 75 mm, or 100 mm. Lauric acid is selected as the working PCM due to its favourable melting temperature and thermophysical stability, and its properties are summarized in Table 1. Note that the average melting temperature is set to be $T_m = 319$ K (45.85 °C) in this paper, which is the average of the solidus temperature and the liquidus temperature.

2.2. Governing equations

To simplify the simulation of heat transfer in latent heat thermal energy storage systems with natural convection, the following assumptions are adopted.

Table 1
Thermophysical properties of lauric acid [43,44] as the PCM.

Thermophysical properties	Lauric acid
Density solid/liquid ρ (kg/m^3)	940/885
Thermal conductivity solid/liquid k (W/m·K)	0.16/0.14
Specific heat capacity solid/liquid c_p (J/kg·K)	2180/2390
Thermal expansion coefficient β (1/K)	0.0008
Dynamic viscosity μ (Pa·s)	0.0059
Melting point T_m (K)	316.65–321.35
Latent heat h_{sf} (J/kg)	187,210

- The enclosure is sufficiently deep in the out-of-plane (z) direction to suppress sidewall effects, allowing the problem to be treated as two-dimensional.
- The liquid phase of the PCM is modelled as an incompressible, Newtonian fluid with laminar flow.
- The Boussinesq approximation is applied to account for buoyancy-driven flow.
- Thermophysical properties of the PCM are considered temperature-independent within each phase but may differ between the solid and liquid phases.
- The phase change interface is modelled using an enthalpy-porosity approach, where a narrow region represents the phase transition from solid to liquid.
- Heat losses to the environment, radiation, and viscous dissipation are neglected.

Under these assumptions, the flow and heat transfer in the liquid PCM domain are governed by the incompressible Navier–Stokes equations and the energy conservation equation:

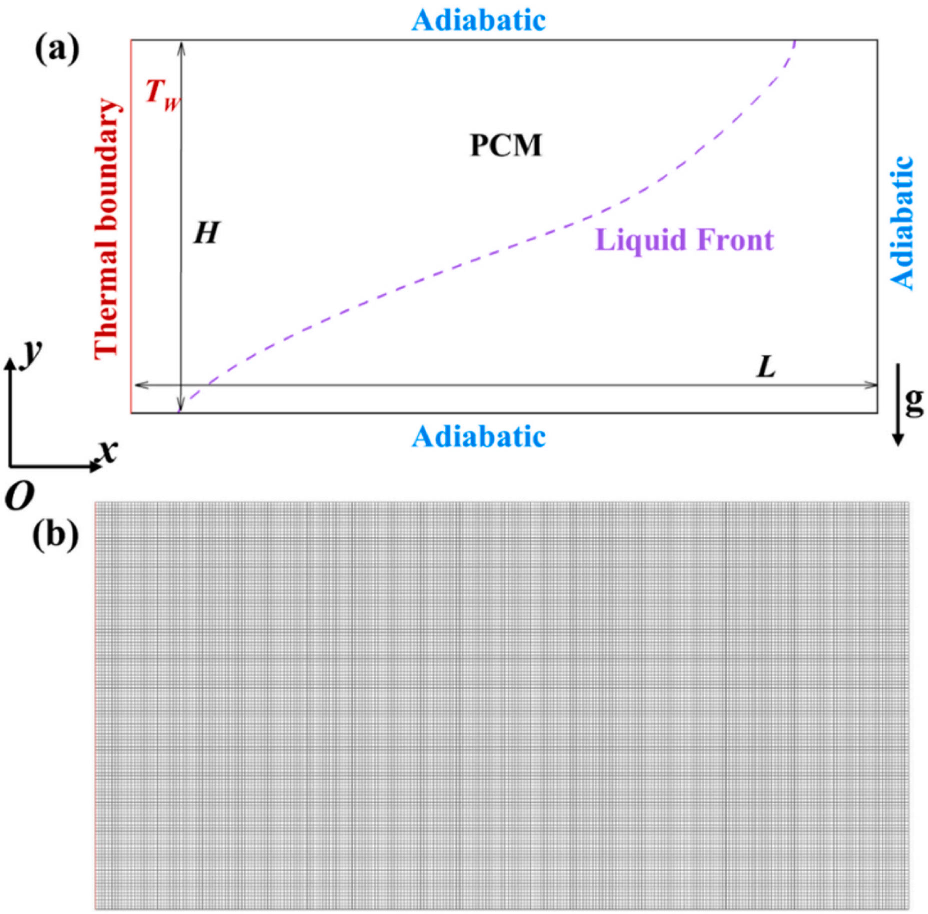

Fig. 1. Schematic of a PCM enclosure with its computational mesh.

$$\nabla\cdot\boldsymbol{u} = 0 \tag{1}$$

$$\left(\frac{\partial\rho\boldsymbol{u}}{\partial t} + \boldsymbol{u}\cdot\nabla(\rho\boldsymbol{u})\right) = -\nabla p + \nabla\cdot\mu\left(\nabla\boldsymbol{u} + \nabla\boldsymbol{u}^T\right) - C\frac{(1-\gamma)^2}{\gamma^3+\sigma}\boldsymbol{u} + \boldsymbol{G} \tag{2}$$

where, in Eq. (2), the second last term uses the Carman-Kozeny equation to mimic the momentum sink through a porous medium [45]. C is the mushy zone constant that comes from the morphology of the mushy region [46] and for this study, it will be obtained through a series of simulations compared to published experimental data in Section 2.4. σ is an extremely small but non-zero number ($\sim 10^{-3}$) used to prevent the singularity of division by 0. γ is the liquid fraction of the PCM, which can be approximated using the following calculation equation:

$$\gamma = \begin{cases} 0, T \le T_s \ (solid\,phase) \\ \dfrac{T-T_s}{T_l-T_s},\ T_s < T < T_l \ (mushy\ zone) \\ 1, T \ge T_l (liquid\,phase) \end{cases} \tag{3}$$

here subscripts s and l represent solid and liquid, respectively while T_s and T_l stand for solidus and liquidus temperature, respectively. The last source term of Eq. (2) is decided by gravity and can be calculated as:

$$\begin{cases} G_x = 0 \\ G_y = \rho g\beta(T - T_m) \end{cases} \tag{4}$$

where T_m (K) is the melting temperature of the PCM, while β (1/K) is the PCM's thermal expansion coefficient, which characterizes the density change with temperature. For heat transfer within the PCM domain, enthalpy formulation is used to account for heat transfer. The total enthalpy can be represented by the sum of latent heat of fusion and the sensible enthalpy, that is,

$$\frac{\partial(\rho h)}{\partial t} + \nabla\cdot(\rho h\boldsymbol{u}) = \nabla\cdot(k\nabla T) \tag{5}$$

$$h = h_{ref} + \int_{T_{ref}}^{T} c_p dT + \gamma h_{sf} \tag{6}$$

where k and c_p are the thermal conductivity and Specific heat capacity of PCM, respectively.

2.3. Boundary conditions

The enclosure is initially at a uniform temperature of 298.15 K (25 °C), which is below the melting point of the phase change material. During the simulation, the left vertical wall is maintained at a constant temperature, T_w, which is set higher than the PCM melting temperature and varied parametrically between 323.15 K (50 °C) and 373.15 K (100 °C) to assess its influence on melting behaviour. The remaining three walls—the right vertical wall and both horizontal walls—are assumed to be perfectly adiabatic, with zero heat flux. A no-slip velocity condition is imposed on all solid boundaries to capture the flow behaviour of the melted PCM phase accurately.

2.4. Numerical procedure

The governing equations are discretised and solved using a pressure-based finite volume method implemented in the commercial CFD software ANSYS FLUENT 19.2. Time integration is performed using a fully implicit scheme to ensure numerical stability. Pressure–velocity coupling is handled via the SIMPLE (Semi-Implicit Method for Pressure Linked Equations) algorithm. Spatial discretization employs a second-order central difference scheme for diffusion terms, while the QUICK (Quadratic Upstream Interpolation for Convective Kinetics) scheme is used for convection terms to enhance solution accuracy. The pressure field is interpolated using the PRESTO! (Pressure Staggering Option) scheme, which improves pressure resolution in regions of strong buoyancy.

The two-dimensional computational domains are discretised using a structured Cartesian mesh. Grid and time step independence studies were performed for a representative case of pure PCM melting under identical boundary conditions. Simulations were conducted using three mesh resolutions (0.4 mm, 0.5 mm, and 0.8 mm) and three time step sizes (0.05 s, 0.10 s, and 0.15 s), with results shown in Fig. 2(a) and (b). For these tests, the enclosure dimensions were set to $H = 50$ mm and $L = 120$ mm, while the heated wall temperature was maintained at 343.15 K. Based on the convergence of the melt fraction and temperature field, a grid size of 0.25 mm (corresponding to 96,000 control volumes) and a time step of 0.1 s were selected for all subsequent simulations to ensure both accuracy and computational efficiency.

To accurately model the phase change process with natural convection, the mushy zone constant, C, was calibrated against published experimental data [43]. The reference experiment employed a rectangular enclosure under conditions identical to those described in Section 2.1. Numerical simulations were conducted using the previously validated grid and time step sizes, and several values of C were tested. As shown in Fig. 3, it was found that $C = 1 \times 10^6$ kg/(m^3·s) yields the closest agreement with the experimental measurements. Accordingly, this value was adopted for all subsequent simulations in this study.

3. Results and discussion

The melting behaviour of a rectangular PCM enclosure heated from one side is governed by the interplay between conduction and natural convection. In the limiting case of pure conduction, the melt front remains parallel to the heated wall, and the melting rate depends solely on the diffusive distance, i.e., the enclosure length (L). However, in practical scenarios, natural convection dominates the heat transfer within the liquid PCM reservoir, significantly enhancing the melting rate compared to pure conduction. The melt front initially elongates as it approaches the insulated wall, after which it progressively shrinks, resulting in a transition to conduction-dominated behaviour and a marked slowdown in phase change progression.

While the convective-dominant melting process is more complicated, our investigation will first concentrate on analysing melting numerically and analytically; afterwards, the analytical results will then extend to the solidification process. To investigate the impact of enclosure size on the melting, a parameter study with different Lengths (L) and Heights (H) is conducted. Like introduced in section 2, the left wall is isothermally heated with a constant temperature while the other three walls are adiabatic. A dimensional analysis of these case reveals the Prandtl number (Pr), Grashof number (Gr) and the Rayleigh number (Ra), where the H is used as the characteristic length:

$$Pr = \frac{\nu}{\alpha};\ Gr = \frac{g\beta(T_w - T_m)H^3}{\nu^2};\ Ra_H = Pr\cdot Gr$$

These depends on the thermal diffusivity $\alpha = k/(\rho C_p)$, kinematic viscosity $\nu = \mu/\rho$, the gravity constant g, the thermal expansion coefficient β, the temperature difference between the heating wall boundary and the melting temperature of PCM. The relating material properties are list in Table 1. Then, for a fixed thermal boundary $T_w = 343.15$ K and initial PCM temperature $T_0 = 298.15$ K, the dimensions of rectangular enclosures and the corresponding non-dimensional groups are given in Table 2. The Prandtl numbers are constant for all cases with values of 100.7.

3.1. Effect of enclosure length

To start with, we first introduce the heat flux within a sufficient wide

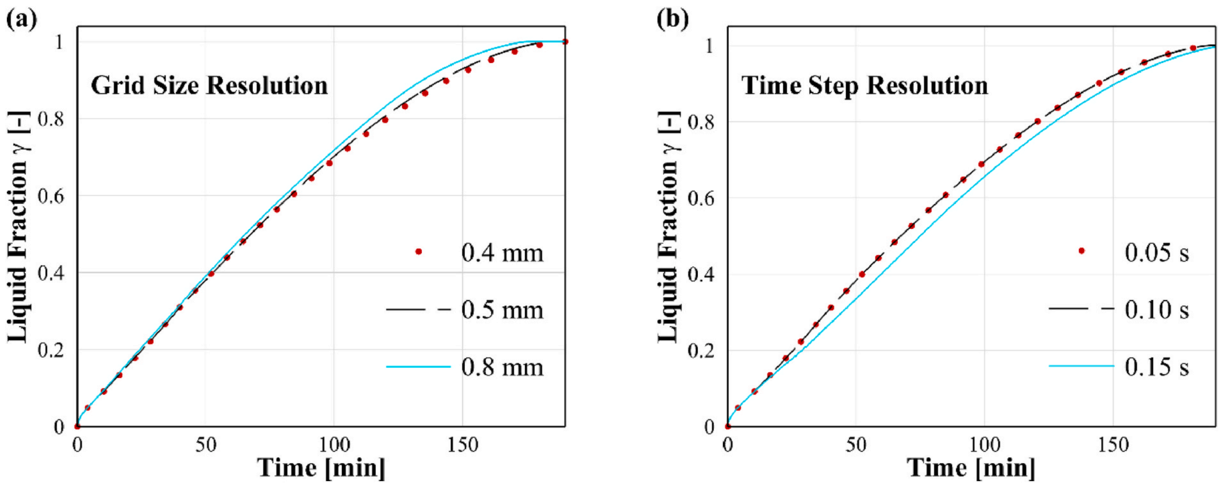

Fig. 2. Independent test of grid size resolution (a) and time step resolution (b).

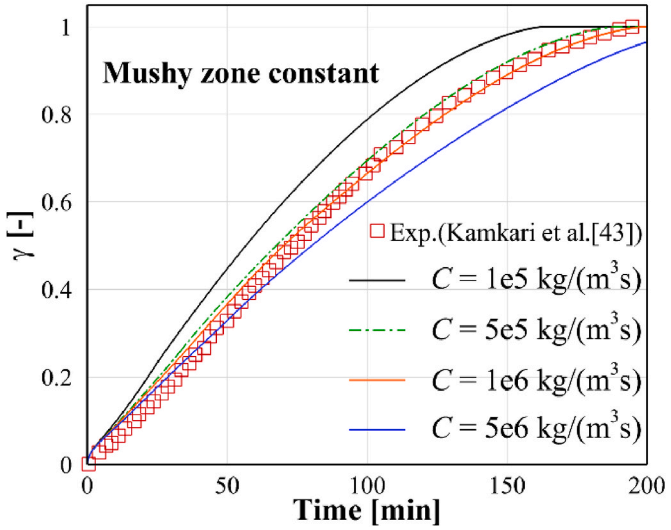

Fig. 3. Liquid fraction evolutions under different numerical mushy zone constants in comparison with experimental measurement [43].

Table 2
Dimensions, aspect ratios and Rayleigh-numbers of representative cases.

Case #	L [mm]	H [mm]	$AR = H/L$	Ra_H
Case 0	50	12.5	0.25	$8.9\bullet10^5$
Case 1	25	12.5	0.5	$8.9\bullet10^5$
Case 2	75	12.5	0.167	$8.9\bullet10^5$
Case 3	100	12.5	0.125	$8.9\bullet10^5$
Case 4	50	4	0.08	$2.9\bullet10^5$
Case 5	50	10	0.2	$4.5\bullet10^5$
Case 6	50	25	0.5	$7.1\bullet10^6$
Case 7	50	50	1	$5.7\bullet10^7$
Case 8	50	100	2	$4.6\bullet10^8$

Note that Table 2 only lists representative cases for Figs. 4–9. Approximate seventy more cases will be extensively studied with varying L and H as well as wall temperatures for Figs. 10 and 11.

enclosure (to enable convection) during melting:

$$q = h\cdot(H\cdot 1)\cdot\Delta T \tag{7}$$

Here, h represents heat transfer coefficient (nearly constant for the convection regime), H is the enclosure height, $\Delta T = T_w - T_m$ is temperature difference. With fixed enclosure height, the heat flux is constant, where the entire melting time will be constrained by the enclosure length (L), which is approximated as

$$t_{melt} = \frac{Q}{q} \sim \frac{\rho(H\cdot L\cdot 1)h_{sf}}{h(H\cdot 1)(T_w - T_m)} \sim \frac{1}{Nu_H \alpha Ste}HL \tag{8}$$

where $Ste = c_p\Delta T/h_{sf}$ and $Nu_H \sim Ra_H^{1/4}$. Then, to study the thermal impact due to natural convection, the convective enhancement factor ω can be introduced:

$$\omega_\gamma = \frac{q''_\gamma}{q''_{cond,\gamma}} \tag{9}$$

where $q'' = \int k_w \frac{dT}{dx}|x = 0\,dy/\int dy$ is the actual heat flux through the left wall with natural convection and q''_{cond} is the hypothetical heat flux by conduction only [27,28].

Fig. 4 illustrates the variation of the liquid fraction over time for enclosures with different lengths (L = 25 mm, 50 mm, 75 mm, and 100 mm) at a fixed height of 12.5 mm. As seen, the melting time increases with increasing enclosure length, corresponding to Eq. (8). Moreover, linear trends of liquid fraction over time have been observed for all cases, suggesting that convective heat transfer dominates the melting

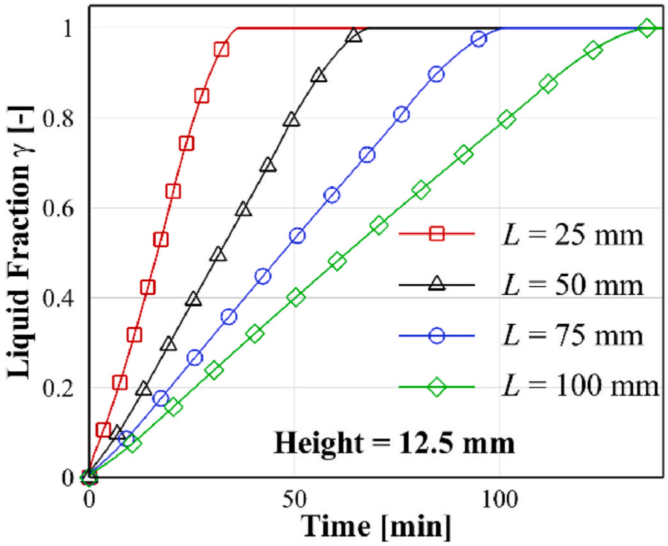

Fig. 4. Evolutions of liquid fraction during melting for Cases 0–3 under fixed enclosure height of 12.5 mm.

process.

The temporal evolution of melt fronts for a fixed enclosure height of 12.5 mm but varying lengths is illustrated in Fig. 5. Each dashed line corresponds to a time instant $t_n = n \times \Delta t$, where $\Delta t = 10$ min. The final time instant indices n for each case are 3 (Case 1, $\gamma = 0.91$), 6 (Case 0, $\gamma = 0.94$), 9 (Case 2, $\gamma = 0.94$), and 12 (Case 3, $\gamma = 0.93$). These indices scale proportionally with their respective enclosure lengths being 25, 50, 75, and 100 mm, corroborating the scaling relation of $t_{melt} \sim L$, derived in Eq. (8). Note that in Fig. 5(a)–(d), the final time index shown does not necessarily correspond to the exact instant of complete melting. Each case requires an additional period for the residual "shrinking solid" to fully disappear. For cases (a)–(c), this additional time is less than one $\Delta t = 10$ min, while for case (d) it extends between one and two Δt. To enable a consistent comparison, we therefore selected the time index at which the liquid fraction γ is approximately equal across the cases. For Case 3, this corresponds to $n = 12$ ($\gamma \approx 0.93$) rather than the last plotted index ($n = 13$, $\gamma \approx 0.98$). Moreover, the liquid fraction difference between neighbouring melt fronts remains approximately constant, corresponding to near-linear evolutions of liquid fraction in Fig. 4, which indicates nearly constant heat flux q (and thus equivalent h under constant H) in Eq. (7).

Fig. 6 illustrates the variations of (a) heat flux (in W/m^2) and (b) convective enhancement factor (ω) as functions of the liquid fraction (γ) for different enclosure lengths ($L = 25$ mm, 50 mm, 75 mm, and 100 mm) at a fixed height of 12.5 mm. As shown in Fig. 6(a), all heat flux curves exhibit a sharp initial decline from their respective maximum values within the very early stage ($\gamma \approx 0$–0.02). This is followed by a short-term increase during the interval $\gamma \approx 0.02$–0.1, where the heat flux momentarily recovers. Subsequently, a long-term plateau is observed for γ ranging approximately from 0.1 to 0.8, during which the heat flux decreases gently with a relatively mild slope. Finally, as the liquid fraction exceeds $\gamma \approx 0.8$ and approaches full melting, the heat flux undergoes a rapid decline until the end of the phase change process.

As shown in Fig. 6(b), the convective enhancement factor (ω) initially increases approximately linearly with the liquid fraction (γ), reflecting the progressive intensification of natural convection during melting. After reaching its peak, ω rapidly declines to a lower value as the available liquid region for convection diminishes. Both the rates of increase and subsequent decrease in ω become steeper as the enclosure length (L) increases. Furthermore, the peak position of ω is progressively delayed with increasing L, e.g., Case 1 ($\gamma \approx 0.7$), Case 0 ($\gamma \approx 0.8$), Case 2 ($\gamma \approx 0.84$), and Case 3 ($\gamma \approx 0.9$), indicating that larger enclosures sustain convective enhancement over a longer fraction of the melting process.

3.2. Effect of enclosure height

To investigate the effect of enclosure height on melting dynamics, a set of cases with a fixed enclosure length of $L = 50$ mm was examined, as shown in Fig. 7, where the heated wall temperature was held constant at 70 °C (343.15 K). For most heights, the melt fraction increased approximately linearly with time, but the rate of increase diminished progressively when the height exceeded 9 mm. Notably, the case with $H = 4$ mm initially exhibited a melting rate comparable to that of $H = 10$ mm. However, beyond 20 min, a significant reduction in melting rate was observed for the $H = 4$ mm case, such that the $H = 50$ mm case—despite its initially slower melting rate—surpassed it at approximately 75 min. Furthermore, one notices that the melting time is not always decreasing with H, an optimal valve should be sought along with influencing parameters.

Next, temporal evolutions of the melting front for cases with three heights ($H = 4$, 10, and 50 mm) under fixed enclosure length are presented in Fig. 8. Again, each dashed curve denotes the solid-liquid interface with a certain liquid phase fraction (γ) at a time instant $t_n = n \times \Delta t$ with the time interval being $\Delta t = 10$ min. In the case with $H = 4$ mm (Fig. 8(a)), the melting fronts primarily advance in the horizontal direction, with nearly parallel contours indicating lowest natural convection strength, compared to other contours. When the height increases to $H = 10$ mm (Fig. 8(b)), natural convection becomes more pronounced, leading to the upward transport of heated fluid toward the top of the enclosure and a rapid progression of the melt front along the upper region. This results in a sloped phase front, driven by a vertical temperature gradient. As the height further increases to $H = 50$ mm (Fig. 8(c)), the phase front becomes increasingly inclined, and the melting near the left-bottom corner progresses slowly. In this case, the dominant mode of heat transfer becomes vertical stratified convection, with a stronger influence of thermal gradients across the y direction. This shift in melting behavior will be explained mathematically in next section.

The evolutions of heat flux and convective enhancement factor with respect to the liquid fraction are presented in Fig. 9 for various enclosure heights. As shown in Fig. 9(a), the heat flux from the heated wall increases notably with height. For the smallest height ($H = 4$ mm), the heat flux decreases gradually throughout the melting process, with overall values remaining relatively constant. As the height increases, however, the heat flux exhibits an initial increase followed by a pronounced decline. In particular, for $H = 25$ and 50 mm, the heat flux initially exceeds that of $H = 10$ mm but eventually drops to similar levels. This behavior can be explained by referring to Fig. 8: prior to the

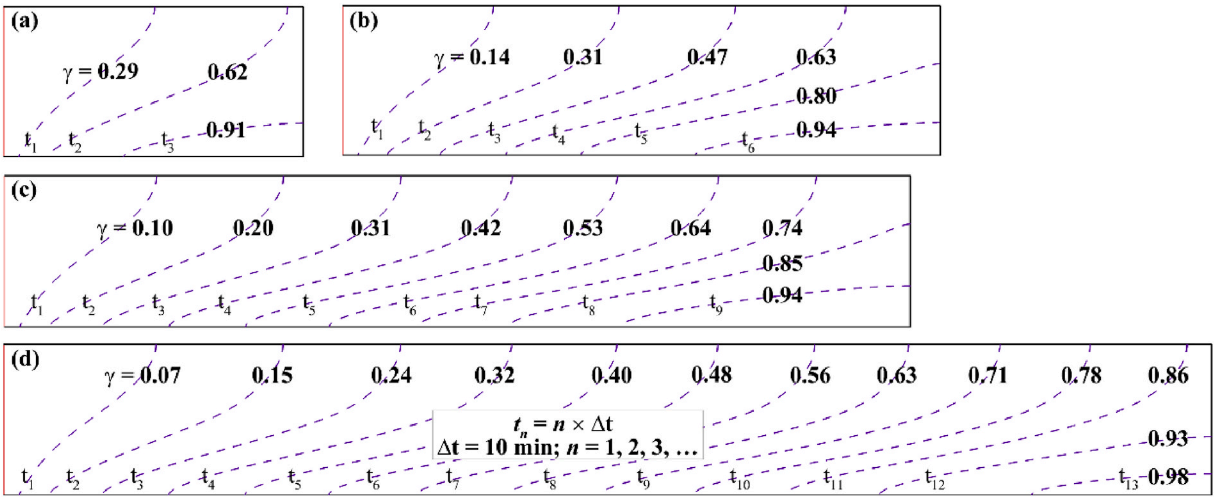

Fig. 5. Melt fronts for Cases 0–3 with different enclosure lengths under fixed height of 12.5 mm: (a) Case 1; (b) Case 0; (c) Case 2; and (d) Case 3. Note that the dash line represents the melt front at the time instant of $t_n = n \times \Delta t$, where $n = 1, 2, 3, \ldots$and $\Delta t = 10$ min.

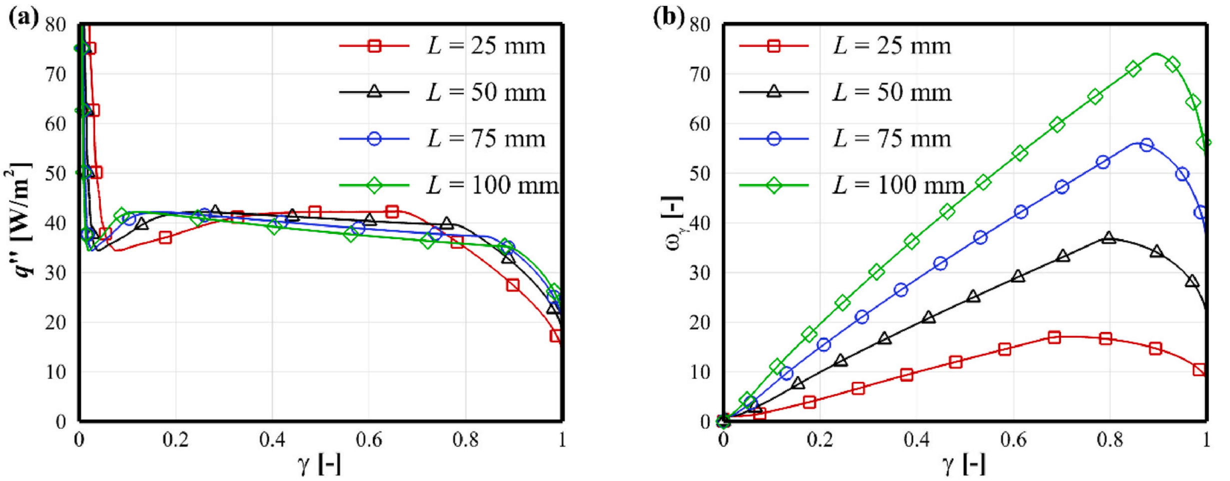

Fig. 6. The heat flux (a) and convective enhancement factor (b) versus liquid fraction for Case 0–3 with different enclosure lengths and fixed height of 12.5 mm.

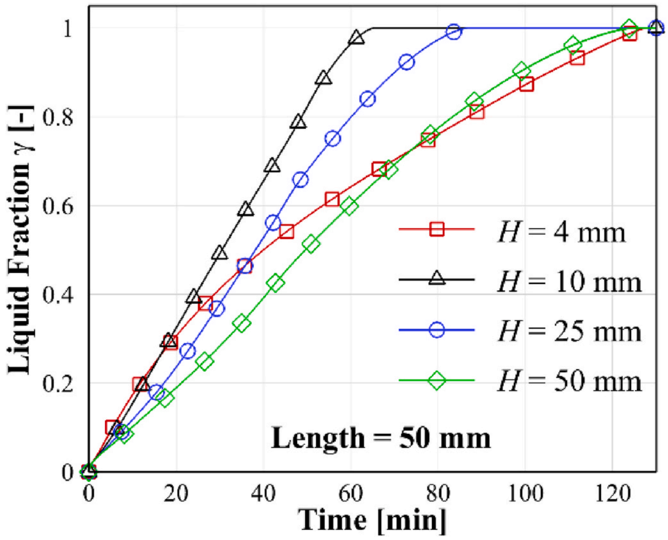

Fig. 7. Evolutions of liquid fraction during melting for Cases 4–7 under fixed enclosure length of 50 mm.

melt front reaching the right boundary, the interface becomes increasingly inclined, increasing its length beyond the left wall length and enhancing the heat transfer through natural convection. This results in a slow rise in heat flux. Once the interface contacts the right wall, the effective length of the solid–liquid boundary begins to decrease, eventually becoming shorter than the left boundary. Since the heat flux is proportional to the interfacial length, a rapid decline follows.

Fig. 9(b) shows the variation of the convective enhancement factor, ω, with the liquid fraction. For $H = 4$ mm, the curve first increases from unity to around 12 (which means that the convective heat transfer is twelve times higher than conductive heat transfer) at $\gamma = 0.3$–0.4, followed by a plateau with a nearly constant ω value until the end of melting. By contrast, curves of $H = 10$, 25, and 50 mm show a pattern of reverse parabolic, indicating that the melting pattern shift corresponding to Fig. 8(b) and (c). Compared with Cases of $H = 4$ and 50 mm, one observes that the convective enhancement factor ω for $H = 50$ mm remains lower than that of $H = 4$ mm up to $\gamma = 0.35$ approximately. Beyond this point, ω for $H = 50$ mm surpasses that of $H = 4$ mm and maintains a higher value until around $\gamma = 0.95$. This corresponds to the slope change of relevant curves, leading to the liquid fraction of the $H = 50$ mm case coincides with that of the $H = 4$ mm at around $\gamma = 0.72$. More importantly, it shows that different peak values of ω are observed

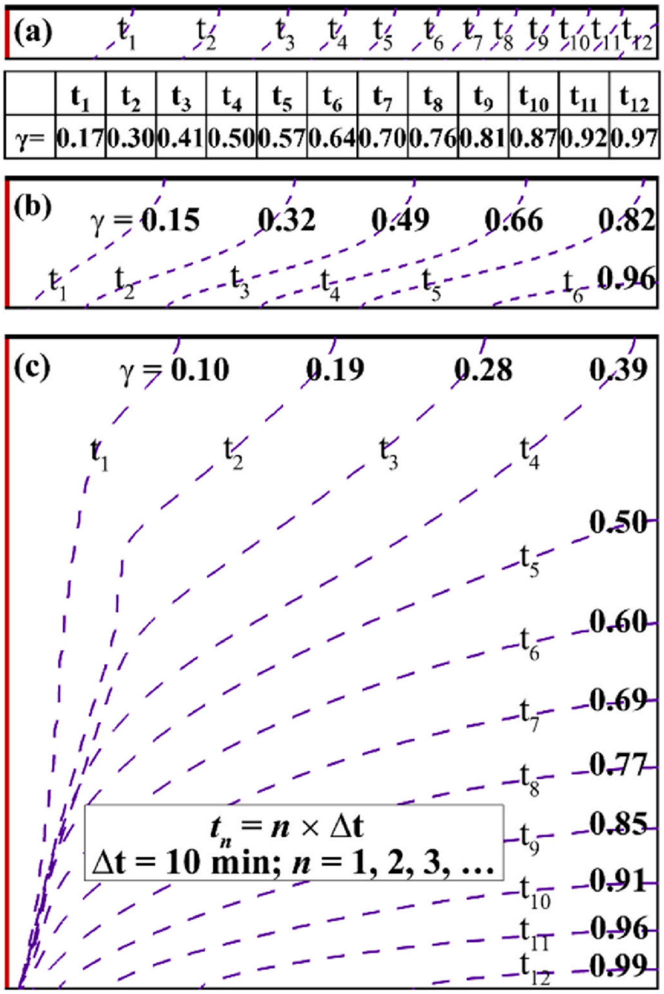

Fig. 8. Melt fronts for Cases with different enclosure heights under fixed length of 50 mm: (a) Case 4 ($H = 4$ mm); (b) Case 5 ($H = 10$ mm); and (c) Case 7 ($H = 50$ mm). Note that the dash line represents the melt front at the time instant of $t_n = n \times \Delta t$, where $n = 1, 2, 3, \ldots$and $\Delta t = 10$ min.

as 39, 30 and 19, for $H = 10$, 25, and 50 mm Cases. This perfectly explains why the $H = 10$ mm Case has the lowest melting time, as shown in Fig. 7.

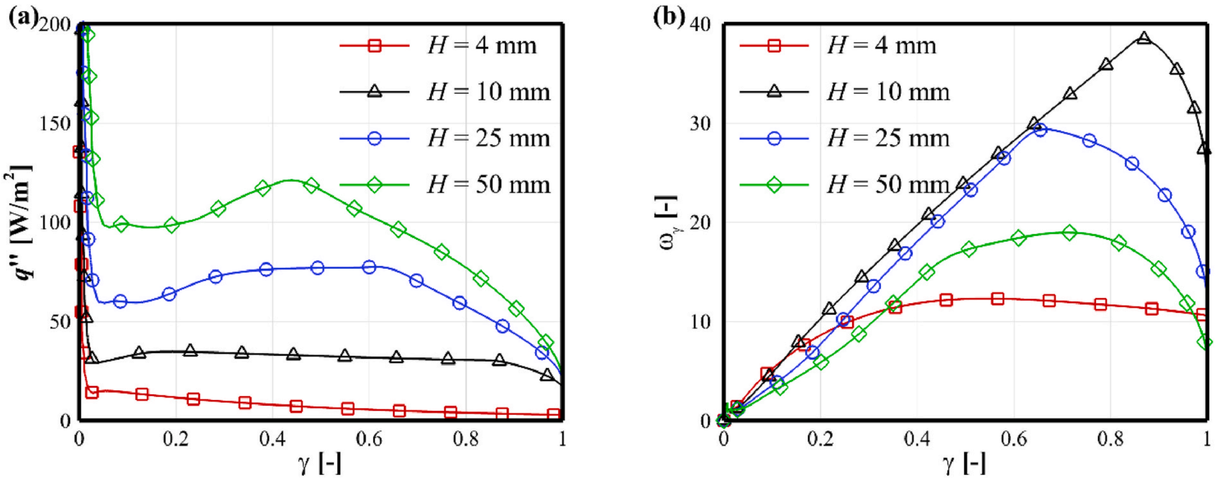

Fig. 9. The heat flux (a) and convective enhancement factor (b) versus liquid fraction for Cases 4–7 with different enclosure heights and a fixed length of 50 mm.

3.3. Optimal enclosure height

Under a fixed enclosure length, Eq. (8) suggests that the melting time decreases with increasing enclosure height, following the relation $t_{melt} \sim H^{1/4}$ [27]. However, this scaling gradually becomes invalid as the height becomes too small to sustain natural convection, indicating the existence of an optimal enclosure height. To further investigate this behavior, the melting times for cases with varying enclosure lengths and heights are plotted in Fig. 10. As anticipated, the melting time initially decreases with increasing height, reaches a minimum, and then begins to rise. In contrast to previous experimental studies [43], the present results suggest the existence of a distinct optimal enclosure height, at which the combined effect of natural convection and thermal resistance is balanced to yield the shortest melting time.

As shown in Fig. 10 (a), for cases with the smallest enclosure length (e.g., $L = 25$ mm), the melting time decreases sharply as the height H increases from nearly zero to approximately 5 mm, indicating a rapid transition from conduction-dominated melting to a convection-enhanced regime. In this low-height range, where conduction dominates, the melting process is slow, leading to prolonged melting times. As the height increases, natural convection strengthens and significantly accelerates the melting. This trend continues until an optimal height is reached, beyond which further increases in H result in a gradual rise in melting time. This behavior is attributed to a shift in the melting paradigm: during melting, the solid–liquid interface reorients from vertical (with a length equal to the enclosure height, H) to inclined (approaching the diagonal of the enclosure) and eventually to horizontal (with a length equal to the enclosure length, L). In confined geometries, the convected liquid PCM rapidly reaches the right boundary. Once the melt front contacts the right wall, its length begins to decrease, leading to a reduction in the effective heat transfer area. The convective plume sweeps across an increasingly flattened melt front, normal to the heated wall, resulting in a decline in convection enhancement factor (ω) and thus the melting rate. Therefore, the total melting time becomes approximately proportional to the enclosure height, with the melt front progressing vertically and undergoing minimal morphological change.

Furthermore, as exhibited in Fig. 10(b), the optimal enclosure height (H_{opt} in mm) along with its corresponding minimum melting time (t_{min} in min) linearly increase with the enclosure length (L in mm), as follows

$$H_{opt} = 0.072 \times L + 5.00 \left(R^2 = 0.9818\right) \tag{10a}$$

$$t_{min} = 1.403 \times L - 4.63 \left(R^2 = 0.9999\right) \tag{10b}$$

With these correlations, thermal engineers can easily estimate the optimal enclosure height and its corresponding melting time for a given enclosure length, providing a practical tool for predictive thermal storage design. These trends suggest that both the geometric configuration and melting performance of enclosures can be effectively scaled, offering valuable design guidance for modular PCM-based thermal storage systems used in heat commodification applications.

While the above correlations are specifically derived for $T_w = 70$ °C

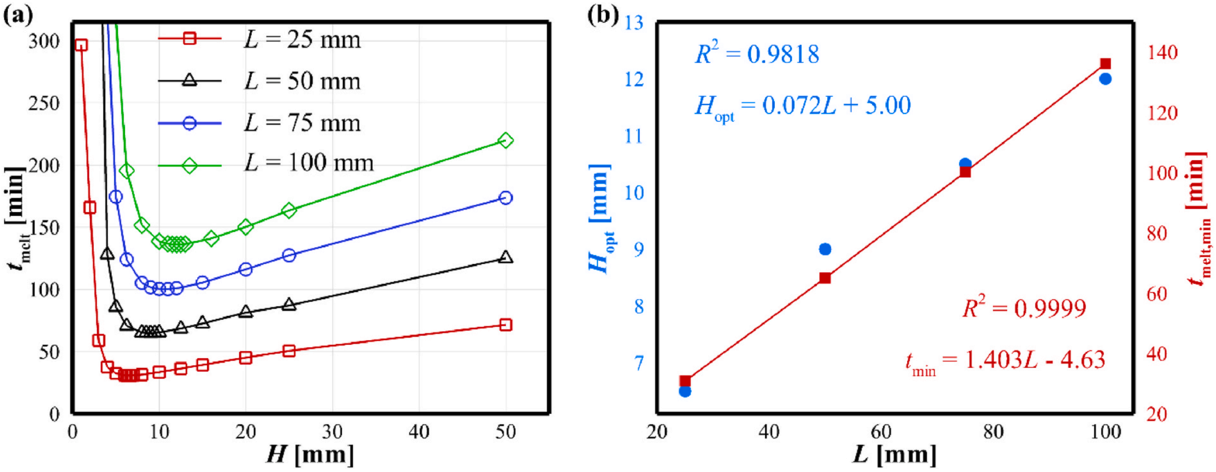

Fig. 10. (a) Melting time (t_{melt}) variations versus H with various L value under constant $\Delta T = 35$ K; and (b) Optimal height (H_{opt}) along with melting time versus L.

($\Delta T = 24.15$ K), additional simulations were conducted across a range of wall temperatures to widen the applicability. As shown in Fig. 11(a), the optimal enclosure height is plotted against enclosure length (L) for several temperature differences ($\Delta T = T_w - T_m$). When ΔT is small (e.g., 4.15 K), the optimal height increases sharply with length—from approximately 8 mm (at $L = 25$ mm) to 17 mm (at $L = 100$ mm)—indicating that weaker thermal driving forces require a taller enclosure to sustain convective enhancement. As ΔT increases, this growth in H_{opt} with length becomes less pronounced. In fact, for larger temperature differences (≥44.15 K), the optimal height becomes nearly constant across all lengths. This indicates that if Eq. (10) is calibrated based on a sufficiently high thermal threshold (e.g., $\Delta T = 44.15$ K), further recalibration is unnecessary for higher operating temperatures, as the optimal height becomes insensitive to additional thermal increases.

Corresponding to each optimal height H_{opt}, the minimum melting time t_{min} versus enclosure length (L) is plotted in Fig. 11(b), for various temperature differences ΔT. As seen, t_{min} increases monotonically with L for each ΔT. At lower ΔT (e.g., 4.15 K), the melting time is significantly longer, reaching over 1200 min at $L = 100$ mm. As ΔT increases, the minimum melting time t_{min} reduces dramatically due particularly to enhanced convective heat transfer. For higher ΔT (e.g., 44.15 and 54.15 K), the melting time becomes almost insensitive to further increases in ΔT. Fig. 11(c) presents the variation of the optimal aspect ratio ($AR_{opt} = H_{opt}/L$) with respect to the temperature differences (ΔT), for four different enclosure length ($L = 25, 50, 75, 100$ mm). All curves exhibit a rapid decline in aspect ratio at lower ΔT while the AR_{opt} values remain relatively unchanged for $\Delta T \geq 44.15$ K. Moreover, as the enclosure length L increases, the optimal aspect ratio AR_{opt} generally increases as well. For larger enclosures (e.g., $L = 100$ mm), the aspect ratio is consistently lower across all ΔT, highlighting that longer enclosures require relatively shorter optimal heights for efficient performance. Fig. 11(d) is an extension of Eq. (10b) for multiple ΔT with a linear coefficient K_t. As seen, it decreases sharply as ΔT increases initially. As ΔT increases beyond 24–35 K, K_t rapidly drops and begins to level off, reaching nearly constant values (~2.5–3) at higher temperature differences (e.g., 44.15–54.15 K).

4. Scale analysis

In this section, a theoretical model to obtain the optimal height of a rectangular PCM box is presented. The reasons for the existence of this optimal height or aspect ratio are first explained, and a possible mathematical model is developed to predict the optimal values. Then, the theoretical model is validated against the numerical results.

As discussed in the introduction, several scholars have suggested inserting impermeable, adiabatic horizontal partitions into high-aspect-ratio PCM enclosures, thereby dividing them into multiple tanks with reduced height, in order to enhance the heat transfer rate during charging (melting). However, the underlying mechanisms of this enhancement remain insufficiently theoretically explained, and while the optimal height of the segmented vertical layers has been numerically obtained in previous studies, it has not been clearly elucidated. In this

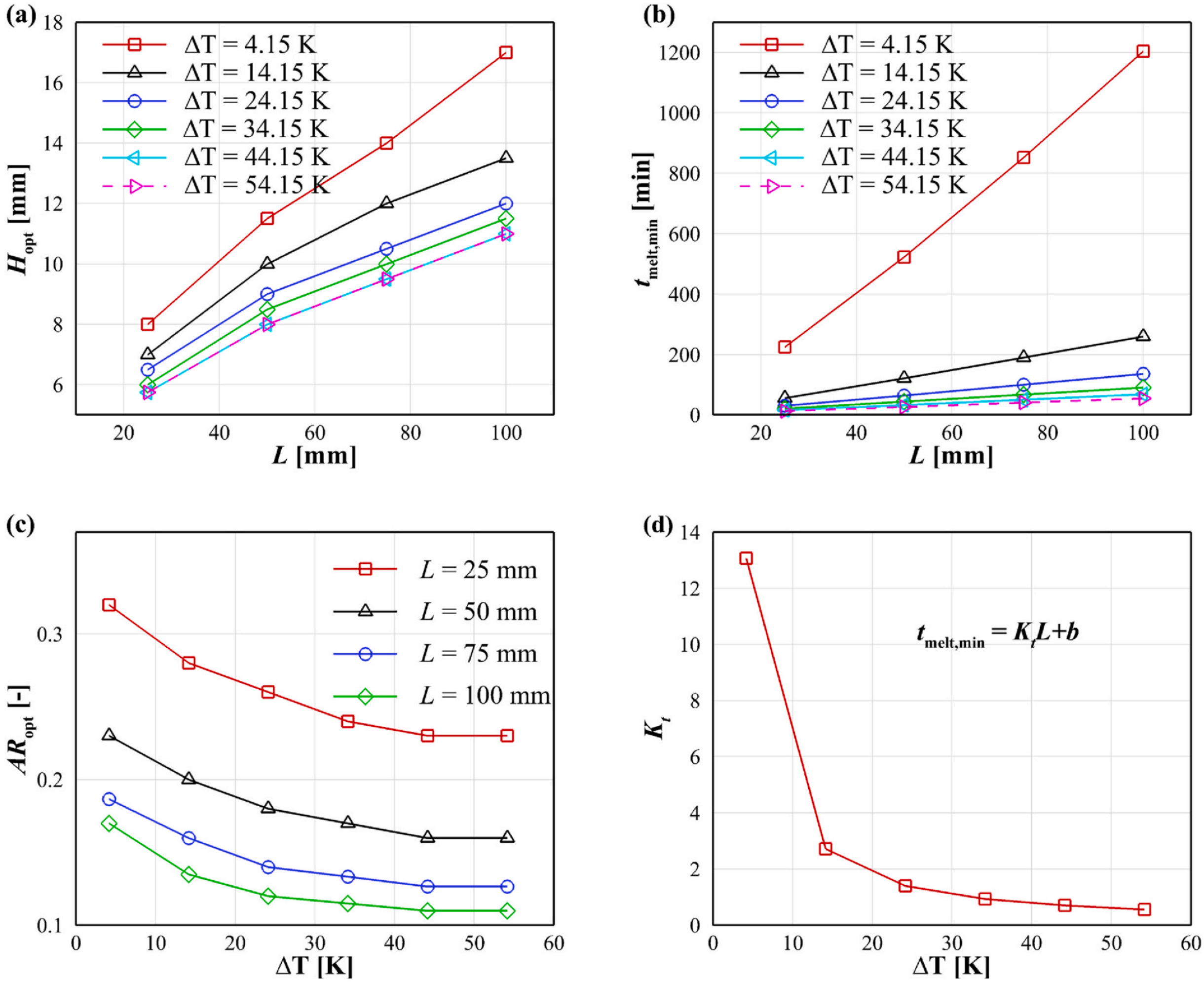

Fig. 11. (a) Optimal height (H_{opt}) and (b) t_{min} versus enclosure length (L) under different temperature differences (ΔT); as well as (c) optimal aspect ratio (AR_{opt}) and (d) the linear coefficient for t_{min} (K_t) versus temperature differences (ΔT).

study, we consider a rectangular PCM enclosure that is isothermally heated from one side while the other three sides are kept adiabatic. The buoyancy circulation cell that is driven by the temperature difference (ΔT in this paper) will be immediately generated and grows. Note that this phenomenon is different from that of a PCM box isothermally heated from the bottom, where there is a critical value of melting layer thickness (or critical Rayleigh number, 1708) for the onset of liquid motion and convective heat transfer. Moreover, for the Rayleigh-Bernard flow (basal heating scenario), there are many convective cells emerging, growing, and merging with each other as the melting proceeds, while the lateral heating case normally only has one convective roll. Fig. 12 shows the segmentation of a tall PCM into multiple short systems with adiabatic and equidistant horizontal partitions.

To simplify the dynamic melting problem, we referred to the four heat transfer regimes (Conduction, Tall systems, Boundary layer regime, and Shallow systems) [47] for natural convection in an enclosure that is isothermally heated from the side, depending on the enclosure aspect ratio ($AR = H/L$) and height-based Rayleigh number ($Ra_H = g\beta(T_w - T_m)H^3/(\alpha\nu)$). From the heat transfer perspective, the optimal height of the segmented vertical layers is equivalent to maximizing overall heat transfer rate (or averaged Nusselt number) to achieve the shortest melting time. To examine geometric effect on melting procedure paradigms, two extreme scenarios are studied, which are the tall ($AR\rightarrow \infty$) and shallow ($AR\rightarrow 0$) enclosures, as shown in Fig. 13(a) and (b). Fig. 13 (c) signifies the most enclosures with aspect ratios within the range between zero and infinity [48].

4.1. Tall enclosure ($AR\rightarrow\infty$)

For this case, the convective regime of four melting stages model is largely extended, and the melting front advances become downwards. As shown in Fig. 13(a), all heat by vertically convected plume jets is absorbed by the nearly horizontal melt front.

$$k\frac{H}{\delta_T}(T_w - T_m) \sim \rho L h_{sf}\frac{dh}{dt} \tag{11}$$

where the thermal boundary layer thickness δ_T can be expressed as $HRa_H^{-1/4}$. Therefore, by ignoring the other three stages (conduction stage, transition stage and 'shrinking solid' stage), the melting duration scale of extreme tall system scenario can be written as

$$t_{melt} \sim \frac{L^{7/4}}{\alpha \times Ste \times Ra_L^{1/4}} H^{1/4} \tag{12}$$

4.2. Shallow extreme ($AR\rightarrow 0$)

Under such conditions, the vertical thermal diffusion is far greater than the enthalpy flow in the horizontal direction at both end regions ($x = 0$ *or* L). The analogy is counterflow heat exchanger where the friction force is balanced with the buoyancy as the inertia goes to zero. The energy conservation is expressed as

$$\overline{Nu}\, k\frac{H}{L}(T_w - T_m) \sim \rho H h_{sf}\frac{ds}{dt} \tag{13}$$

where the expression of conduction referenced Nusselt number is $\overline{Nu} = 1 + \frac{1}{9!}\left(AR^8 Ra_L^2\right)$ [47]. The melt front movement is in the *horizontal* direction as shown in Fig. 14. The melting time is scaled as

$$t_{melt} \sim \frac{L^2}{\alpha \times Ste \times \left(1 + AR^8 Ra_L^2/9!\right)} \tag{14}$$

Fig. 14 compares the analytical predictions of melting time with simulation results across various enclosure lengths. When the aspect ratio $AR\rightarrow 0$, corresponding to very shallow enclosures, the simulated data agrees closely with the analytical model. This consistency is expected, as the analytical prediction assumes negligible natural convection, a condition that holds when the enclosure height is sufficiently small, and conduction dominates the melting process. However, even a slight increase in height introduces buoyancy-driven flow, and the deviation between simulation and theory becomes apparent. This reflects the growing influence of natural convection, which is not accounted for in analytical derivation. Conversely, at larger heights (i.e., when $AR\rightarrow\infty$), the simulation results begin to follow the analytical trend more closely again, although some discrepancies remain—particularly in the higher H range. The simulation data exhibits a near-linear increase in melting time with height, while the analytical solution approaches an asymptotic limit.

It is noted that in the present study, the maximum aspect ratio is approximately 2, which does not fully reach the high-AR asymptotic regime assumed in the theoretical model. Therefore, while the analytical solution provides useful bounding behavior, a full convergence between the models is not yet observed. Further exploration into the high-*AR* regime will be addressed in future work.

4.3. Intersection of asymptotes: optimal segmented height

The underlying rationale for the existence of an optimal enclosure height can be understood as the balance between two dominant heat-transfer processes. 1) Along the top surface, fluid parcels heated at the hot wall are convectively transported toward the solid–liquid interface

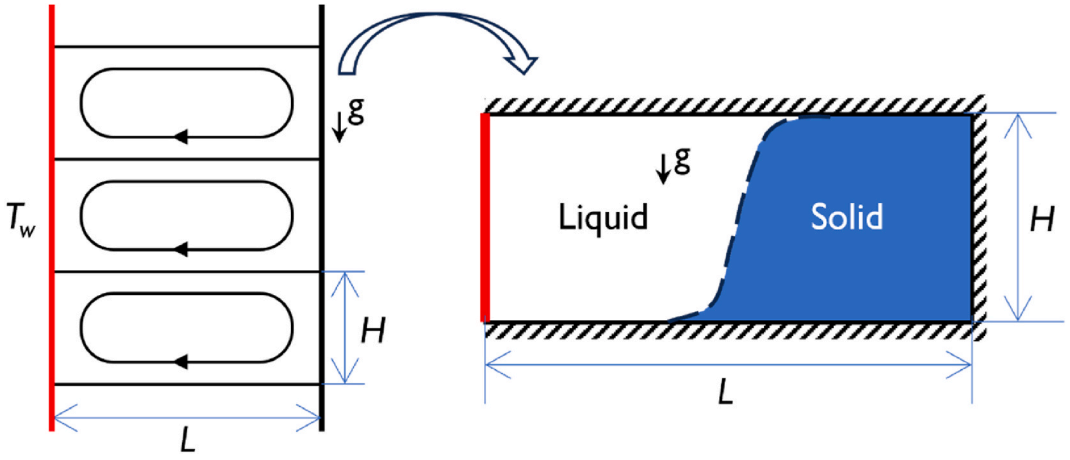

Fig. 12. Segmentation of a tall PCM into multiple short systems with adiabatic and equidistant horizontal partitions.

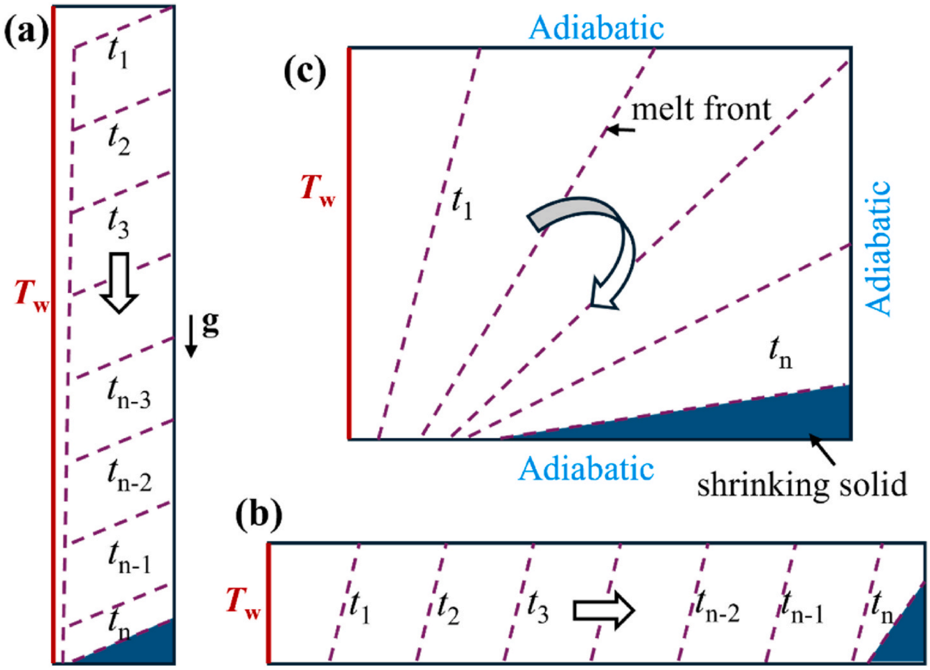

Fig. 13. Three classification enclosures with various melting paradigms: (a) tall enclosure; (b) shallow enclosure; (c) rectangular enclosure.

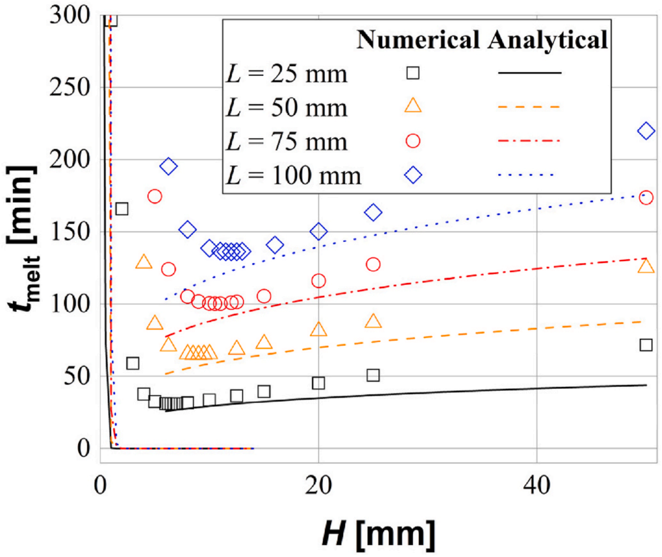

Fig. 14. Comparisons of numerical t_{melt} and analytical predictions based on Eqs. (12) and (14).

($Q_{conv,\rightarrow} = \overline{Nu}\,k(T_w - T_m)$). 2) Along the right near-vertical solid–liquid interface, these parcels exchange heat with the melt front while descending (($Q_{cond,\downarrow} = k\frac{L}{H}(T_w - T_m)$). Once cooled, they are deflected near the bottom and return toward the hot wall, forming a convective roll. As shown in Section 3.1, the heat carried by the fluid parcels is not dissipated during this transport, and the convective-regime heat flux remains nearly independent of the enclosure length (Fig. 6(a)). This interaction implies that an optimal enclosure height (Hopt) exists, where the lateral convective transport and the vertical counterflow are dynamically balanced ($Q_{conv,\rightarrow} \sim Q_{cond,\downarrow}$). If H is larger than H_{opt}, many fluid parcels are cooled down the melting temperature before reaching the bottom, causing very slow melting near the bottom corner (Fig. 13(b) → Fig. 13(a)). Conversely, if H is smaller than H_{opt}, the buoyancy-driven natural convection is weakened that leads to a reduction in $Q_{conv,\rightarrow}$; meanwhile, the downward conductive heat transfer $Q_{cond,\downarrow}$ increases, and the overall heat transport gradually shifts toward a conduction-dominated regime (Fig. 13(c)) (one can refer to Page-239 [47]). All these predictions are consistent with the results in Fig. 8. Hence, the optimal height corresponds to the balance point between these two heat-transfer processes, as expressed by Eq. (15).

Hence, the optimal height, that is estimated as the balance of enthalpy flow at both ends and thermal diffusion of upper-and-bottom counterflows [49], can be written as

$$\overline{Nu}\,k(T_w - T_m) \sim k\frac{L}{H}(T_w - T_m) \tag{15}$$

where the averaged Nusselt number can be estimated as $\overline{Nu} \sim Ra_H^{1/4}$. Therefore, the critical height of the segmented layer is

$$H_{opt} \sim C_H\frac{L}{Ra_L^{1/7}} \text{ or } AR_{opt} \sim C_H Ra_L^{-1/7} \tag{16}$$

Fig. 15 compares the predicted optimal enclosure heights H_{opt} derived from the mathematical model against simulation results for various wall temperature differences, ΔT, across four enclosure lengths. The model incorporates the thermophysical properties of the melted PCM to compute the Rayleigh number, while a correction factor C_H is introduced to account for discrepancies between the idealized formulation and the actual complex melting behavior. In each subplot, the solid black curve represents the simulation-determined H_{opt}, while the colored lines denote the model predictions for three different values of C_H. The shaded region encapsulates the envelope bounded by the highest and lowest predictive curves, providing an estimate of the uncertainty or sensitivity of the model to C_H.

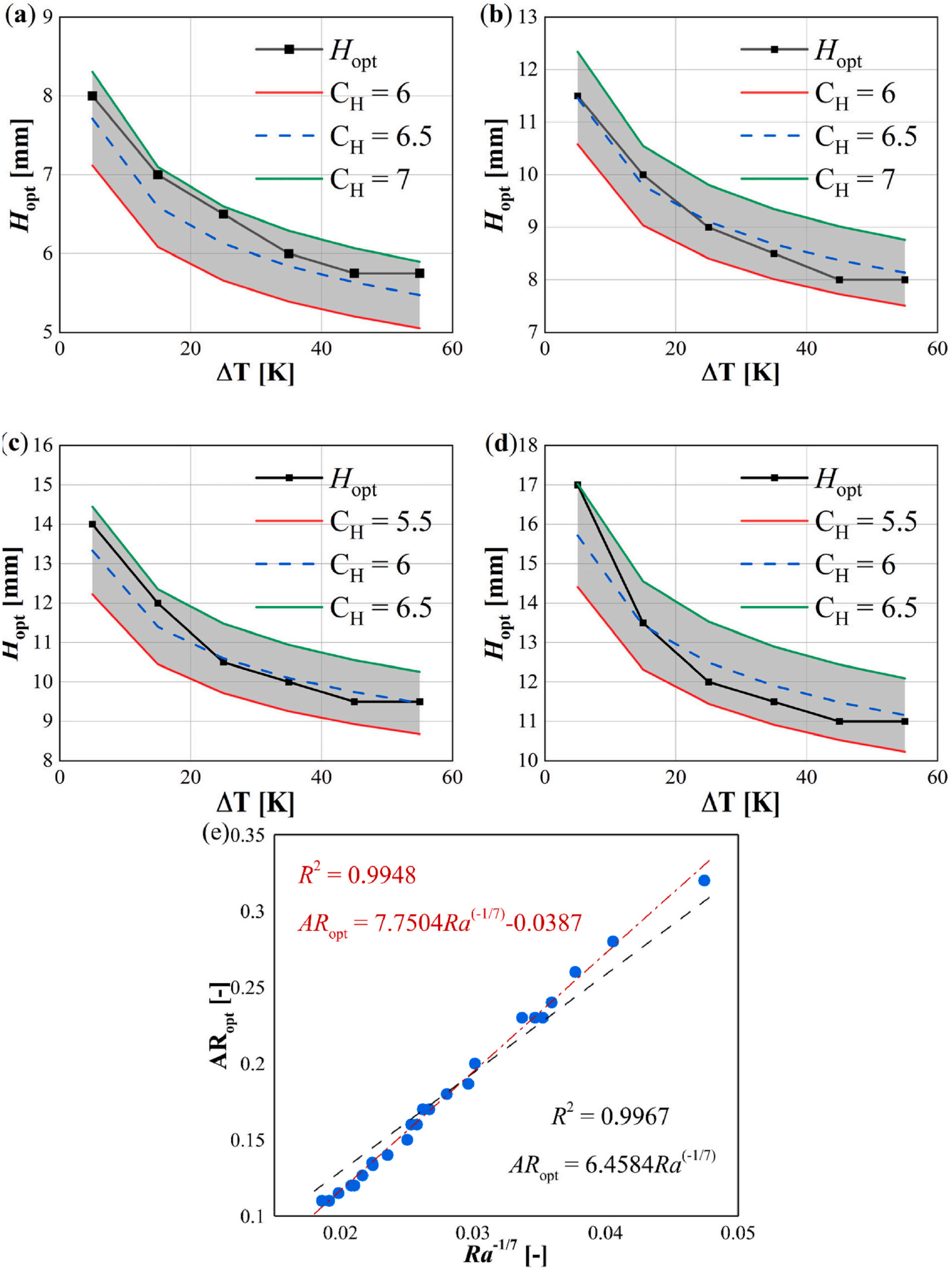

Fig. 15. Comparisons of numerical and analytical results: H_{opt} versus ΔT with various C_H values under: (a) $L = 25$ mm, (b) $L = 50$ mm, (c) $L = 75$ mm, (d) $L = 100$ mm; as well as the fitting correlations for $AR_{opt} \sim C_H Ra_L^{-1/7}$.

Despite its simplicity, the model captures the correct trend of decreasing optimal height with increasing ΔT. For a given enclosure length, H_{opt} declines as ΔT increases, but the rate of decrease diminishes at higher temperatures, indicating a saturation effect. Notably, the predictive model's coefficients—especially the empirical match factor C_H—exhibit a decreasing trend with both increasing temperature and length. When the wall temperature approaches approximately 373.15 K in these cases, the simulated optimal heights begin to plateau, forming nearly horizontal asymptotes. However, the theoretical model continues to predict a gradual decline in H_{opt}, albeit at a reduced rate. At lower temperatures, a higher match factor is required to align the model with the simulation, suggesting increased influence from non-ideal effects not captured in the current formulation. Overall, the proposed model performs reliably within the mid-range of operating conditions, particularly for $\Delta T \in [25,45]$ K, and the prediction accuracy remains within one order of magnitude across all conditions. This validates the utility of the model as a practical tool for rapid estimation, especially when precise numerical simulations are not feasible. Moreover, the range bounded by different C_H values offer a meaningful bracket to assess uncertainty due to non-ideal effects in PCM melting dynamics.

5. Solidification

While the primary focus of this study has been on the melting process, the solidification behavior of phase change materials (PCMs) is also of interest and warrants dedicated analysis. In fact, the physical mechanisms involved during solidification can be viewed as a mirrored scenario of those discussed in Section 4.2 for melting.

During the initial stages of solidification, the domain—entirely in the liquid phase—allows for potentially strong natural convection. However, as solidification progresses, the emerging solid phase behaves as a thermal insulator [50], increasingly impeding heat transfer. This results in a continuous decline in overall discharging rate as the solid front expands inward from the cooling wall. Notably, the extent and influence of this effect are amplified with increasing enclosure length L, as a longer cavity delays the complete transformation and creates a larger thermal resistance path [51,52].

To ensure comparability between melting and solidification processes, we adopt a symmetric temperature boundary setup using the methodology described in Section 2.3. Specifically, we define the cooling wall temperature, T'_w, and the initial temperature of the domain T'_0 during solidification through the following symmetric relationships:

$$T_w - T_m = T_m - T'_w \tag{17}$$

$$T_m - T_0 = T'_0 - T_m \tag{18}$$

Here, $T_0 = 298.15$ K and $T_w = 343.15$ K are the initial and wall temperatures used in the melting simulations, while T_m represents the phase transition temperature of the PCM. Consequently, for solidification, we set $T'_w = 294.85$ K and $T'_0 = 339.85$ K to maintain symmetry around the phase transition point.

Fig. 16 illustrates the variation in total solidification time t_{solid} as a function of enclosure height H for four different lengths $L = 25$ mm, 50 mm, 75 mm, and 100 mm. As the enclosure length increases from 25 mm to 100 mm, the time required for complete solidification increases by nearly an order of magnitude—from approximately 240 min at $L = 25$

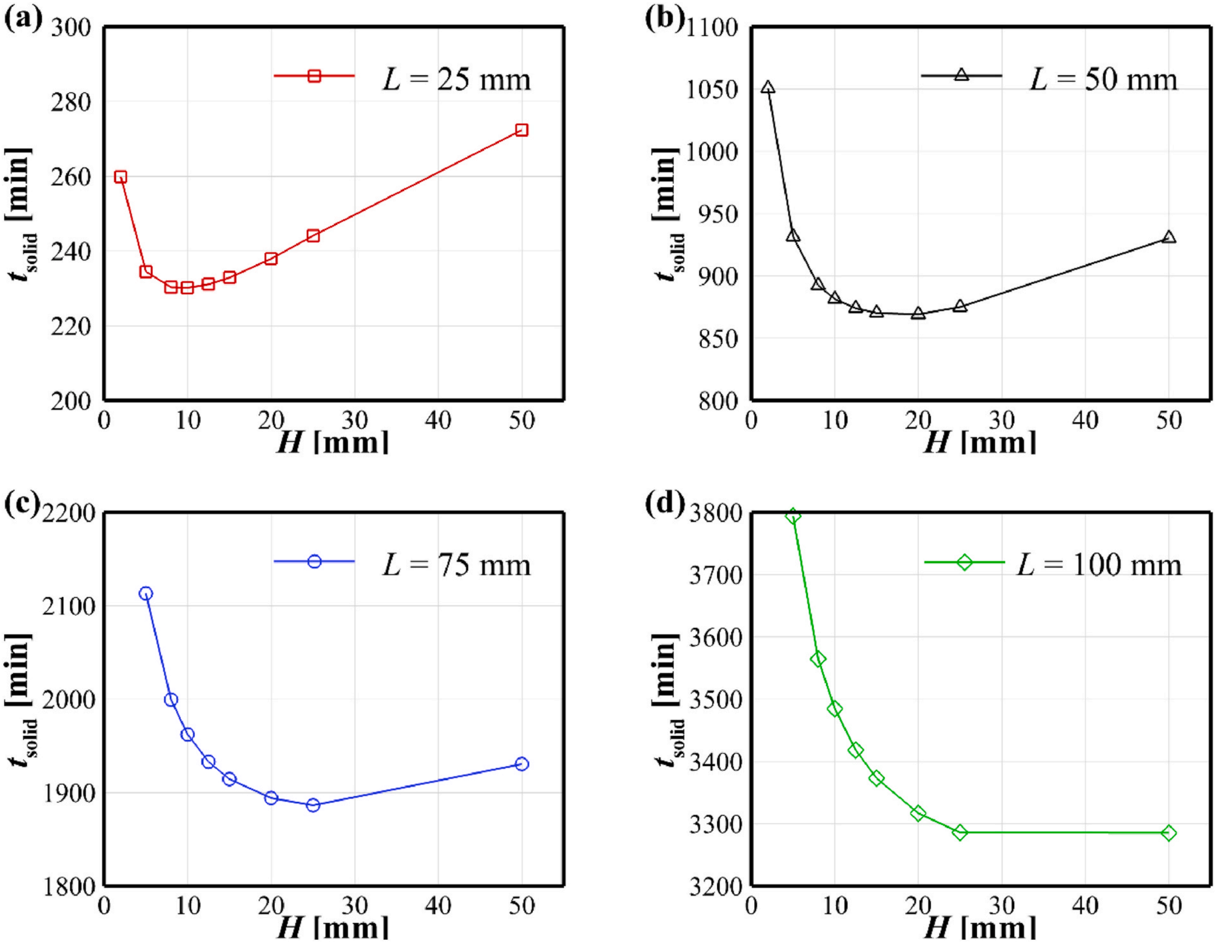

Fig. 16. Solidification time (t_{solid}) variations versus H under constant $\Delta T = 24.15$ K with (a) $L = 25$ mm; (b) $L = 50$ mm; (C) $L = 75$ mm; (d) $L = 100$ mm.

mm to over 3300 min at $L = 100$ mm. This indicates that the thermal resistance introduced by the expanding solid phase during solidification becomes substantially more pronounced with increasing enclosure length.

For each given length, the solidification time exhibits a non-monotonic trend with respect to height. At small H, increasing the height significantly reduces the solidification time, reflecting the enhanced cooling interface and stronger initial convective effects in the liquid phase. However, after a critical height is reached (which varies with L), further increases in height result in a gradual or constant rise in solidification time. This change in behavior is attributed to the diminishing effect of convection once the solid phase dominates the thermal resistance near the cooling wall.

Notably, in the high-height region (i.e., when $H > H_{opt}$), the slope of the t_{solid} vs. H curve decreases noticeably with increasing enclosure length L, as evident from all subfigures in Fig. 16. For L = 25 mm, the solidification time continues to rise with height at a moderate rate after reaching the optimal height; while for $L = 100$ mm, the increase in t_{solid} becomes nearly flat for $H > 20$ mm, indicating a diminishing influence of height. This decreasing slope with increasing L is attributed to the dominant role of thermal resistance in the growing solid region, which can be explained as follows. As the enclosure height H increases, buoyancy-driven natural convection becomes stronger, accelerating the initial stage of solidification. However, once most of the domain has solidified, the remaining melt forms a shrinking triangular reservoir near the adiabatic wall (oppose to the cooling wall). In this regime, the solid–liquid interface becomes inclined, and its length shortens progressively as the reservoir height decreases. Consequently, a larger H leads to a taller remaining liquid column, which must solidify through conduction across a diminishing interfacial area. This geometric constraint offsets the benefits of enhanced convection, ultimately increasing the time required to fully solidify the residual melt. These two effects offsets, resulting in the plateau behavior of solidification time observed at higher H (i.e., 100 mm), as shown in Fig. 16(d).

Fig. 17 illustrates the temporal evolution of the solid–liquid phase front during the solidification process for three different enclosure heights—5 mm, 20 mm, and 50 mm—while the enclosure length is fixed at 50 mm. Each dashed contour represents a constant time step ($t_n = n \times \Delta t$, with $\Delta t = 100$ min), and the associated values of the liquid phase fraction γ progressively decrease from 1 to 0 as solidifying. At each time instant, the liquid fractions for three different H are close, for example at t_7 (700 min), $\gamma = 0.12$ for $H = 5$ mm, $\gamma = 0.09$ for $H = 20$ mm, $\gamma = 0.08$ for $H = 50$ mm. The lower value of γ for a larger H indicates the accelerated solidification rate due to intensified convective heat transfer. However, Fig. 17(c) exhibits an additional melt front (t_8 with $\gamma = 0.03$), this illustrates the adverse effect of increasing height (H) on the

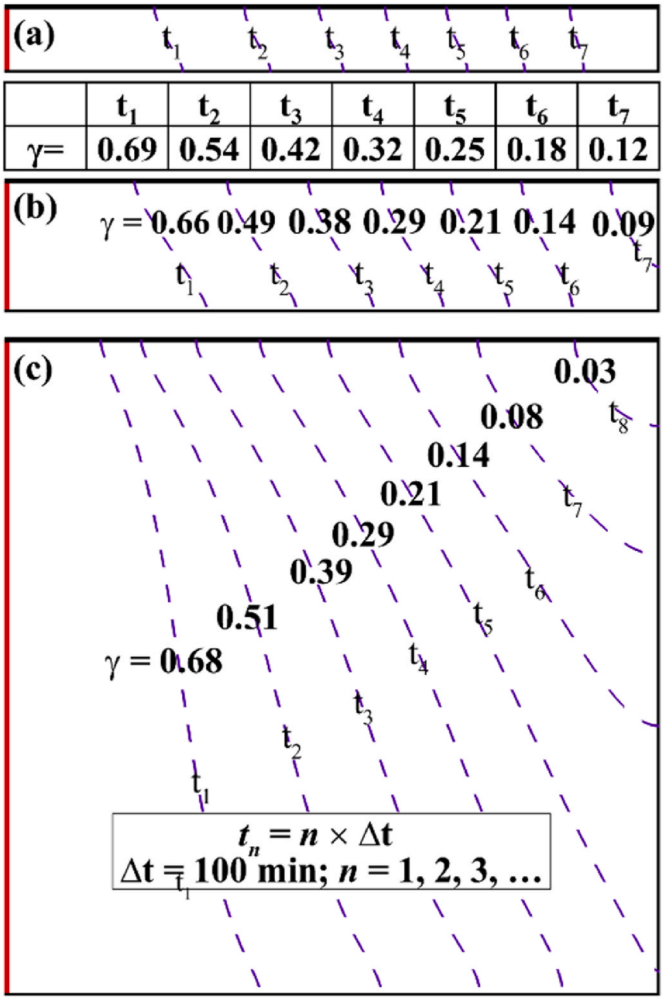

	t_1	t_2	t_3	t_4	t_5	t_6	t_7
γ=	0.69	0.54	0.42	0.32	0.25	0.18	0.12

Fig. 17. Melt fronts for solidification process with different enclosure heights under fixed length of 50 mm: (a) $H = 5$ mm; (b) $H = 20$ mm; and (c) $H = 50$ mm. Note that the dash line represents the melt front at the time instant of $t_n = n \times \Delta t$, where $n = 1, 2, 3, \ldots$ and $\Delta t = 100$ min.

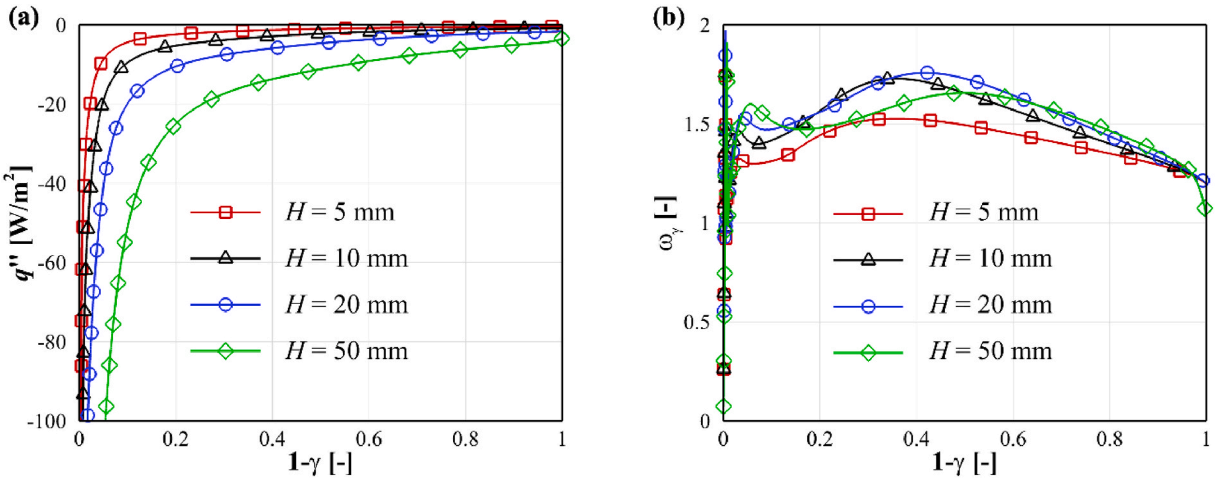

Fig. 18. The heat flux (a) and convective enhancement factor (b) evolutions at $L = 50$ mm during solidification.

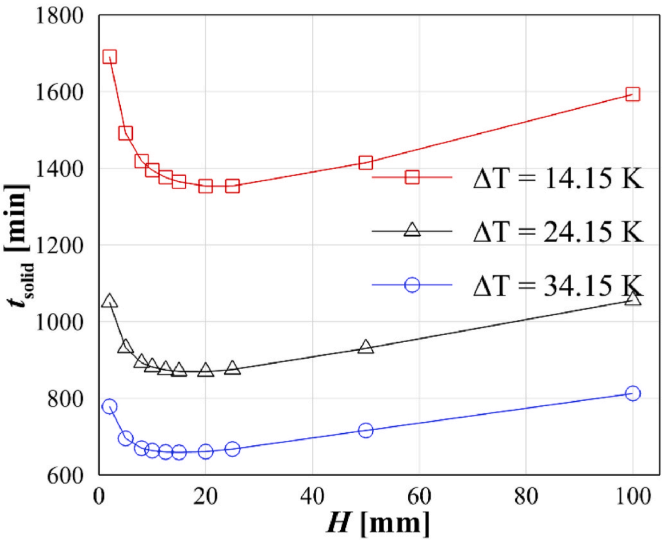

Fig. 19. Solidification time (t_{solid}) versus enclosure height (H) at $L = 50$ mm under different temperature differences $\Delta T = 14.15$, 24.15, and 34.15 K.

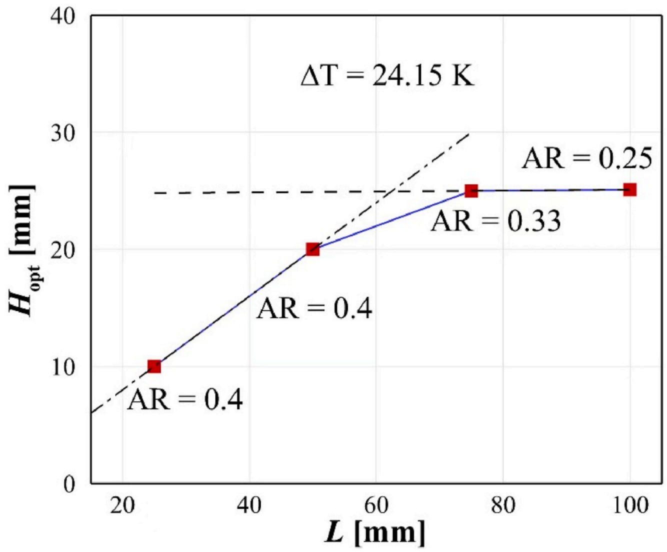

Fig. 20. Optimal enclosure height (H_{opt}) with respect to enclosure length for solidification under constant temperature differences $\Delta T = 24.15$ K.

shrinking of the remaining triangular liquid reservoir.

Fig. 18 illustrates the variation of (a) heat flux q'' and (b) convective enhancement factor ω_γ with the solid fraction (1−γ) during the solidification process for different enclosure heights H. As shown in Fig. 18(a), all cases follow a consistent pattern: the heat flux magnitude drops sharply at the onset of solidification and then gradually decreases toward zero as the process concludes. This trend reflects the declining temperature gradient and the shrinking active heat transfer area. Fig. 18 (b) further reveals that the convective enhancement factor remains below 2 for all heights, indicating that natural convection has only a minor role during solidification. Unlike the melting phase, where ω_γ could reach values exceeding 40, solidification is largely governed by conduction due to the formation of a solidified insulating layer. The presence of residual liquid does enhance heat transfer slightly, especially in the mid-stage ($0.2 < (1-\gamma) < 0.7$), but the effect is marginal. As a result, solidification time is more strongly influenced by enclosure length (L) than height (H), especially in later stages when the convective influence has essentially vanished.

Fig. 19 shows the variation of total solidification time t_{solid} with enclosure height H under different temperature differences $\Delta T = T_0' - T_w'$, where $T_0' = 339.85$ K is fixed and T_w' varies (corresponding to $\Delta T = 14.15$, 24.15, and 34.15 K). The enclosure length is fixed at $L = 50$ mm. Across all cases, the solidification time initially decreases rapidly with increasing height, reaches a minimum at an optimal height H_{opt}, and then gradually increases. This trend reflects a balance between thermal mechanisms: at small heights, limited convection and short vertical heat paths result in longer solidification times dominated by conduction. As H increases, natural convection slightly enhances heat transfer, shortening the time until a minimum is reached. Beyond this point, although convection intensifies, it becomes relatively less effective due to the formation of a shrinking triangular liquid reservoir near the adiabatic wall, which increases the conduction path and slows down solidification. Additionally, increasing ΔT (i.e., lowering the cooling wall temperature) significantly reduces t_{solid} but does not substantially shift the position of H_{opt}. This confirms that while wall temperature affects the total time scale, the underlying geometric and thermal balance controlling solidification dynamics remains consistent.

As mentioned previously, optimal height of the PCM enclosure has been ascertained by two counterbalancing effects. It is therefore reasonably assumed that a convection-impacted region (L_{conv}) exists. For enclosure length is within the same order of magnitude of L_{conv}, the optimal height H_{opt} is expected to increase linearly with enclosure length, maintaining a constant aspect ratio. If the enclosure length is far larger than the L_{conv}, then the solidification time is mainly affected by the shrinking of right-top liquid reservoir through vertical conduction, and the H_{opt} should keep constant. Fig. 20 corroborates the previously predicted trends, which shows the H_{opt} varies with enclosure length under a constant temperature difference $\Delta T = 24.15$ K. More supportive information regarding temperature distribution and isothermals during the solidification can be found in the Appendix.

6. Conclusion

Modular thermal energy storage is a key enabling technology for the emerging heat commodification market, where stacked rectangular tanks filled with phase change materials (PCMs) function as transferable “heat packets.” One of the main challenges for such systems is the inherently low thermal conductivity of PCMs, which limits their charging and discharging rates. While thermal enhancers can improve heat transfer, they typically reduce storage capacity. Inspired by constructal theory, this study proposes an optimized enclosure geometry that leverages natural convection to enhance heat transfer without compromising thermal storage density. The key findings include.

- Increasing the enclosure length leads to a linear increase in melting time. At $H = 12.5$ mm and $\Delta T = 24.15$ K, the heat flux remains constant ($\sim$40 W/m^2) across different lengths (25–100 mm), while the convective enhancement factor—defined as the ratio of actual to conduction-only heat flux—increases with length, reaching maximum values of 75 (for $L = 100$ mm) and 18 (for $L = 25$ mm).
- There exists an optimal height H_{opt} that minimizes melting time. For $L = 50$ mm and $\Delta T = 24.15$ K, the heat flux increases with height, peaking at 120 W/m^2 for $H = 50$ mm. The enhancement factor is highest for $H_{opt} = 10$ mm, with peak values of 12, 39, and 19 for $H =$ 4, 10, and 50 mm, respectively.
- The optimal height increases linearly with L, and decreases with ΔT until $\Delta T = 4.15$ K, beyond which further reduction has minimal effect. The largest $H_{opt} = 17$ mm occurs at $L = 100$ mm and $\Delta T = 4.15$ K, while the smallest $H_{opt} = 5$ mm is observed at $L = 25$ mm and $\Delta T = 44.15$ K. Correspondingly, higher L and lower ΔT yield larger optimal aspect ratios AR_{opt}.
- Corresponding to H_{opt}, the shortest melting time t_{min} increases linearly with L, $t_{min} = K_t L + b$. However, the slope K_t decreases significantly—from 13 to 0.5—as ΔT increases from 4.15 K to 54.15 K.
- Scaling analysis yields predictive correlations for both t_{min} and H_{opt}, which match well with numerical simulations. The optimal aspect ratio for the melting process follows $AR_{opt} \sim 6.5\, Ra_L^{-1/7}$.
- For solidification process, heat transfer is conduction-dominated across all heights, as evidenced by a convective enhancement factor below 2. For large L (e.g., 100 mm), the solidification time becomes nearly independent of H when $H > H_{opt}$, due to the trade-off between enhanced convection and the enlarged residual triangular liquid reservoir.

CRediT authorship contribution statement

Luoguang Zhao: Writing – original draft, Visualization, Validation, Software, Methodology, Investigation, Conceptualization. **Chunrong Zhao:** Writing – original draft, Visualization, Validation, Supervision, Methodology, Investigation, Formal analysis, Data curation. **Michael Opolot:** Writing – review & editing. **Simone Mancin:** Writing – review & editing, Investigation. **Kamel Hooman:** Writing – review & editing, Investigation.

Declaration of competing interest

The authors declare that they have no known competing financial interests or personal relationships that could have appeared to influence the work reported in this paper.

Acknowledgement

The corresponding author, Dr Chunrong Zhao, would like to thank Professor Steven Armfield for the discussion relating to the scale analysis part in this paper.

Appendix

For the solidification process, the buoyancy-driven circulation of the molten PCM rapidly weakens as the growing solid layer impedes heat transfer from the liquid phase to the heated wall. This results in a fast diminished temperature gradient between the liquid PCM and the solid–liquid interface, thereby reducing the overall heat transfer rate [5]. As a result, it is expected that thermal stratification then equilibrium within the liquid PCM region will be quickly achieved after solidification commences. Fig. A1 exhibits temperature fields and isothermals during solidification for different lengths ($L = 25$, 50, 75 and 100 mm) and fixed temperature difference $\Delta T = 24.15$ K. Each figure is displayed with three sets of enclosure heights (shorter than, equal to, and higher than H_{opt}) with four different time instants. As seen in Fig. A1(a), near-vertical isothermals of liquidus temperature persist for larger lengths ($L = 100$ mm), compared to shorter lengths cases. While thermal gradients with the liquid (or more specifically here, mushy zone) are negligible, which confirms conduction-dominated heat transfer, corresponding to Fig. 18(b). Hence, for sufficient long ($L \geq 50$ mm) enclosures, the optimal heights are identical as the trade-off between shorten convection regime (early-stage) and prolonged vertical heat conduction (late stage).

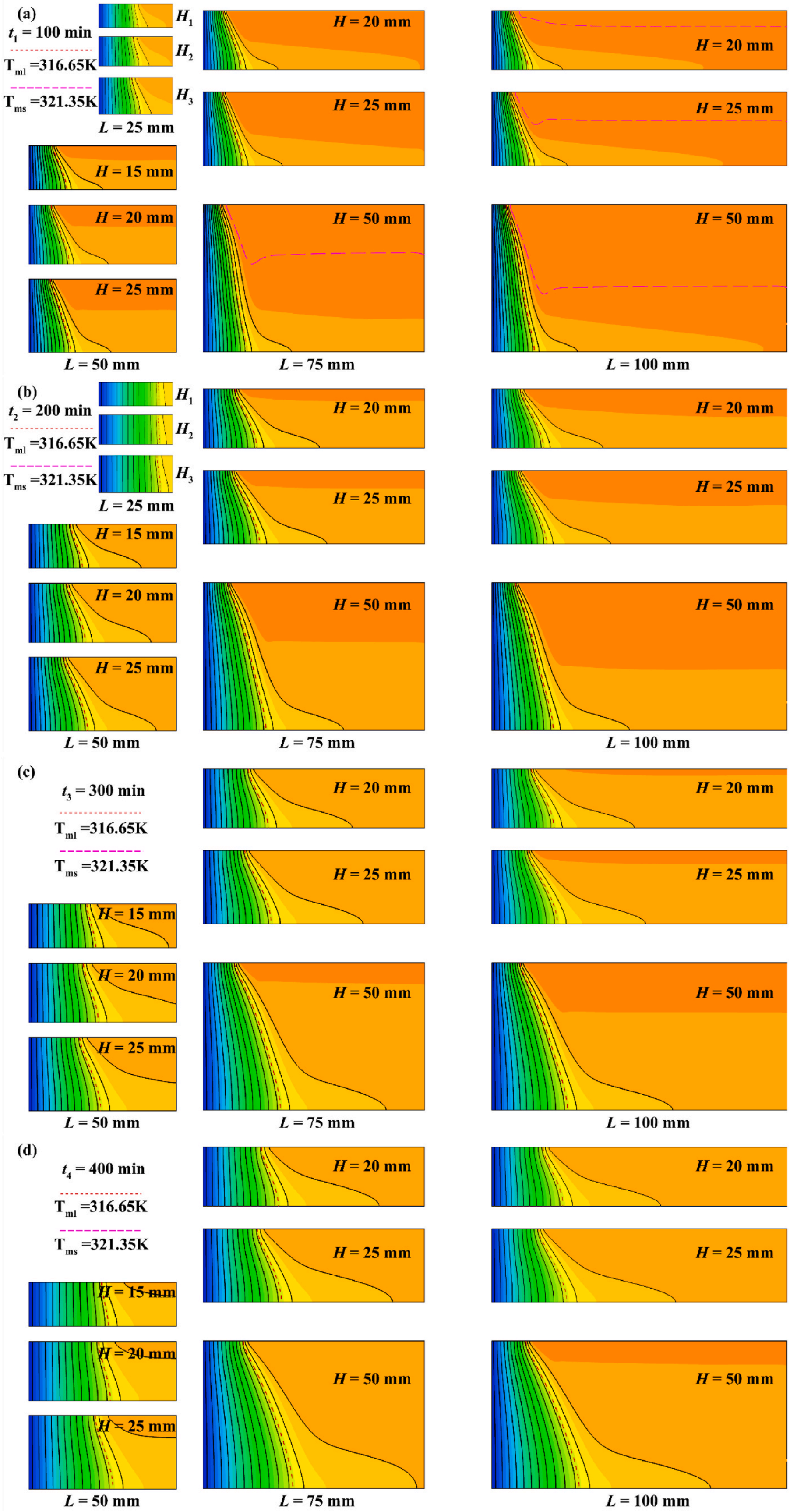

Fig. A1. Temperature fields of the rectangular PCM enclosure with different lengths (25, 50, 75, and 100 mm) and heights (lower than, equal to, and higher than H_{opt}) under fixed temperature difference $\Delta T = 24.15$ K at four different time instants: (a) 100 min, (b) 200 min, (c) 300 min, and (d) 400 min.

Data availability

Data will be made available on request.

References

[1] Kishore RA, Priya S. A review on low-grade thermal energy harvesting: materials, methods and devices. Materials 2018;11(8):1433. https://doi.org/10.3390/ma11081433.

[2] Fisher R, Ciappi L, Niknam P, et al. Innovative waste heat valorisation technologies for zero-carbon ships – A review. Appl Therm Eng 2024;253:123740. https://doi.org/10.1016/j.applthermaleng.2024.123740.

[3] Hooman K. Heat commodification for a sustainable energy future. Power Engineering and Engineering Thermophysics 2024;3(3):189–94. https://doi.org/10.56578/peet030304.

[4] Alva G, Lin Y, Fang G. An overview of thermal energy storage systems. Energy 2018;144:341–78. https://doi.org/10.1016/j.energy.2017.12.037.

[5] Zhao C, Opolot M, Keane P, et al. Thermal characteristics of melting of a phase change material enhanced by a stainless-steel 304 periodic structure. Energy Storage 2023;2(2):442–8. https://doi.org/10.1016/j.enss.2023.02.002.

[6] Ye F, Dong Y, Opolot M, et al. Assessment of thermal management using a phase-change material heat sink under cyclic thermal loads. Energies 2024;17(19):4888. https://doi.org/10.3390/en17194888.

[7] Junior LGS, Ribeiro GB, Mancin S. Effect of fin configuration on the early stage of the melting process of a phase change material. Int J Thermofluids 2024;24:100957. https://doi.org/10.1016/j.ijft.2024.100957.

[8] Kala SM, Ribezzo A, Zsembinszki G, et al. Development of copper metal wool incorporated in a latent thermal energy storage tank for improved charging and discharging. Appl Therm Eng 2025;264:125549. https://doi.org/10.1016/j.applthermaleng.2025.125549.

[9] Zhao C, Sun Y, Wang J, et al. The applicability of volume-averaging method to simulate melting in a multi-scaled periodic structure. Energy 2022;248:123636. https://doi.org/10.1016/j.energy.2022.123636.

[10] Tao YB, He YL. A review of phase change material and performance enhancement method for latent heat storage system. Renew Sustain Energy Rev 2018;93:245–59. https://doi.org/10.1016/j.rser.2018.05.028.

[11] Yang X, Yu J, Guo Z, et al. Role of porous metal foam on the heat transfer enhancement for a thermal energy storage tube. Appl Energy 2019;239:142–56. https://doi.org/10.1016/j.apenergy.2019.01.075.

[12] Zhao C, Opolot M, Liu M, et al. Phase change behaviour study of PCM tanks partially filled with graphite foam. Appl Therm Eng 2021;196:117313. https://doi.org/10.1016/j.applthermaleng.2021.117313.

[13] Alazwari A M, Algarni M, Safaei MR. Effects of various types of nanomaterials on PCM melting process in a thermal energy storage system for solar cooling application using CFD and MCMC methods. Int J Heat Mass Tran 2022;195:123204. https://doi.org/10.1016/j.ijheatmasstransfer.2022.123204.

[14] Nitsas M, Koronaki IP. Performance analysis of nanoparticles-enhanced PCM: an experimental approach. Therm Sci Eng Prog 2021;25:100963. https://doi.org/10.1016/j.tsep.2021.100963.

[15] Zhao C, Wang J, Sun Y, et al. Fin design optimization to enhance PCM melting rate inside a rectangular enclosure. Appl Energy 2022;321:119368. https://doi.org/10.1016/j.apenergy.2022.119368.

[16] Shen Y, Mazhar AR, Zhang P, et al. Structure optimization of tree-shaped fins for improving the thermodynamic performance in latent heat storage. Int J Therm Sci 2023;184:108003. https://doi.org/10.1016/j.ijthermalsci.2022.108003.

[17] Essa MA, Rofaiel IY, Ahmed MA. Experimental and theoretical analysis for the performance of evacuated tube collector integrated with helical finned heat pipes using PCM energy storage. Energy 2020;206:118166. https://doi.org/10.1016/j.energy.2020.118166.

[18] Mohaghegh MR, Alomair Y, Alomair M, et al. Melting of PCM inside a novel encapsulation design for thermal energy storage system. Energy Convers Manag X 2021;11:100098. https://doi.org/10.1016/j.ecmx.2021.100098.

[19] Memon SA, Cui H, Lo TY, et al. Development of structural–functional integrated concrete with macro-encapsulated PCM for thermal energy storage. Applied energy 2015;150:245–57. https://doi.org/10.1016/j.apenergy.2015.03.137.

[20] Velmurugan K, Kumarasamy S, Wongwuttanasatian T, et al. Review of PCM types and suggestions for an applicable cascaded PCM for passive PV module cooling under tropical climate conditions. J Clean Prod 2021;293:126065. https://doi.org/10.1016/j.jclepro.2021.126065.

[21] Shamsi H, Boroushaki M, Geraei H. Performance evaluation and optimization of encapsulated cascade PCM thermal storage. J Energy Storage 2017;11:64–75. https://doi.org/10.1016/j.est.2017.02.003.

[22] Zhao X, Jiaqiang E, Zhang Z, et al. A review on heat enhancement in thermal energy conversion and management using field synergy principle. Appl Energy 2020;257:113995. https://doi.org/10.1016/j.apenergy.2019.113995.

[23] Bejan A, Lorente S. Design with constructal theory. John Wiley & Sons; 2008.

[24] Kamkari B, Groulx D. Experimental investigation of melting behaviour of phase change material in finned rectangular enclosures under different inclination angles. Exp Therm Fluid Sci 2018;97:94–108. https://doi.org/10.1016/j.expthermflusci.2018.04.007.

[25] Jany P, Bejan A. Scaling theory of melting with natural convection in an enclosure. Int J Heat Mass Tran 1988;31(6):1221–35. https://doi.org/10.1016/0017-9310(88)90065-8.

[26] Zhao C, Opolot M, Liu M, et al. Review of analytical studies of melting rate enhancement with fin and/or foam inserts. Appl Therm Eng 2022;207:118154. https://doi.org/10.1016/j.applthermaleng.2022.118154.

[27] Zhao C, Hooman K. Design criteria for advanced latent heat thermal energy storage systems[M]//Solid-Liquid thermal energy storage. CRC Press; 2022. p. 71–96.

[28] Vogel J, Felbinger J, Johnson M. Natural convection in high temperature flat plate latent heat thermal energy storage systems. Appl Energy 2016;184:184–96. https://doi.org/10.1016/j.apenergy.2016.10.001.

[29] Ye WB. Thermal and hydraulic performance of natural convection in a rectangular storage cavity. Appl Therm Eng 2016;93:1114–23. https://doi.org/10.1016/j.applthermaleng.2015.10.083.

[30] Yang X, Wang X, Liu Z, et al. Thermal performance assessment of a thermal energy storage tank: effect of aspect ratio and tilted angle. Int J Energy Res 2021;45(7):11157–78. https://doi.org/10.1002/er.6598.

[31] Yang X, Wang X, Liu Z, et al. Influence of aspect ratios for a tilted cavity on the melting heat transfer of phase change materials embedded in metal foam. Int Commun Heat Mass Tran 2021;122:105127. https://doi.org/10.1016/j.icheatmasstransfer.2021.105127.

[32] Xie S, Wu W. Effect of aspect ratio on PCM melting behavior in a square cavity. Int Commun Heat Mass Tran 2023;143:106708. https://doi.org/10.1016/j.icheatmasstransfer.2023.106708.

[33] He M, Wang H, Ying Q, et al. The effect of aspect ratios and inclination angles on the thermal energy storage of phase change materials in partially filled metal foam. Int Commun Heat Mass Tran 2025;164:108858. https://doi.org/10.1016/j.icheatmasstransfer.2025.108858.

[34] Elbahjaoui R, El Qarnia H. Transient behavior analysis of the melting of nanoparticle-enhanced phase change material inside a rectangular latent heat storage unit. Appl Therm Eng 2017;112:720–38. https://doi.org/10.1016/j.applthermaleng.2016.10.115.

[35] Hamad FA, Egelle E, Gooneratne S, et al. The effect of aspect ratio on PCM melting behaviour in rectangular enclosure. Int J Sustain Eng 2021;14(5):1251–68. https://doi.org/10.1080/19397038.2021.1913533.

[36] Behbahan AS, Noghrehabadi A, Wong CP, et al. Investigation of enclosure aspect ratio effects on melting heat transfer characteristics of metal foam/phase change material composites. Int J Numer Methods Heat Fluid Flow 2019;29(9):2994–3011. https://doi.org/10.1108/HFF-11-2018-0659.

[37] Zhao C, Opolot M, Liu M, et al. Periodic structures for melting enhancement: observation of critical cell size and localized melting. Int J Heat Mass Tran 2022;195:123107. https://doi.org/10.1016/j.ijheatmasstransfer.2022.123107.

[38] Yang X, Lu Z, Bai Q, et al. Thermal performance of a shell-and-tube latent heat thermal energy storage unit: role of annular fins. Applied energy 2017;202:558–70. https://doi.org/10.1016/j.apenergy.2017.05.007.

[39] Zhao C, Opolot M, Liu M, et al. Numerical study of melting performance enhancement for PCM in an annular enclosure with internal-external fins and metal foams. Int J Heat Mass Tran 2020;150:119348. https://doi.org/10.1016/j.ijheatmasstransfer.2020.119348.

[40] Sundarram SS, Li W. The effect of pore size and porosity on thermal management performance of phase change material infiltrated microcellular metal foams. Appl Therm Eng 2014;64(1–2):147–54. https://doi.org/10.1016/j.applthermaleng.2013.11.072.

[41] Parida A, Bhattacharya A, Rath P. Effect of convection on melting characteristics of phase change material-metal foam composite thermal energy storage system. J Energy Storage 2020;32:101804. https://doi.org/10.1016/j.est.2020.101804.

[42] Zhao C, Opolot M, Liu M, et al. Simulations of melting performance enhancement for a PCM embedded in metal periodic structures. Int J Heat Mass Tran 2021;168:120853. https://doi.org/10.1016/j.ijheatmasstransfer.2020.120853.

[43] Kamkari B, Shokouhmand H, Bruno F. Experimental investigation of the effect of inclination angle on convection-driven melting of phase change material in a rectangular enclosure. Int J Heat Mass Tran 2014;72:186–200. https://doi.org/10.1016/j.ijheatmasstransfer.2014.01.014.

[44] Abdi A, Martin V, Chiu JNW. Numerical investigation of melting in a cavity with vertically oriented fins. Appl Energy 2019;235:1027–40. https://doi.org/10.1016/j.apenergy.2018.11.025.

[45] Mahmoudi Y, Hooman K, Vafai K. Convective heat transfer in porous media [M]. CRC Press; 2019.

[46] Shmueli H, Ziskind G, Letan R. Melting in a vertical cylindrical tube: numerical investigation and comparison with experiments. Int J Heat Mass Tran 2010;53(19–20):4082–91. https://doi.org/10.1016/j.ijheatmasstransfer.2010.05.028.

[47] Bejan A. Convection heat transfer[M]. John Wiley & Sons; 2013.

[48] Saha SK, Dutta P. Heat transfer correlations for PCM-Based heat sinks with plate fins. Appl Therm Eng 2010;30(16):2485–91. https://doi.org/10.1016/j.applthermaleng.2010.06.021.

[49] Bejan A. Simple methods for convection in porous media: scale analysis and the intersection of asymptotes. Int J Energy Res 2003;27(10):859–74. https://doi.org/10.1002/er.922.

[50] Opolot M, Zhao C, Liu M, et al. Investigation of the effect of thermal resistance on the performance of phase change materials. Int J Therm Sci 2021;164:106852. https://doi.org/10.1016/j.ijthermalsci.2021.106852.

[51] Mira-Hernández C, Mancin S. Sensitivity of an electrical impedance-based sensor for the liquid fraction estimation during melting and solidification inside a vertical rectangular enclosure. J Phys Conf 2024;2766(1):012018. https://doi.org/10.1088/1742-6596/2766/1/012018. IOP Publishing.

[52] Al-Abidi AA, Mat S, Sopian K, et al. Numerical study of PCM solidification in a triplex tube heat exchanger with internal and external fins. Int J Heat Mass Tran 2013;61:684–95. https://doi.org/10.1016/j.ijheatmasstransfer.2013.02.030.